

Adaptive Entanglement Distillation

Sijie Cheng and Narayanan Rengaswamy

Abstract—Quantum network applications impose a variety of requirements on entanglement resources in terms of rate, fidelity, latency, and more. The repeaters in the quantum network must combine good methods for entanglement generation, effective entanglement distillation, and smart routing protocols to satisfy these application requirements. In this work, we focus on entanglement distillation in a linear chain of quantum repeaters. While conventional approaches reuse the same distillation scheme over multiple hop lengths after entanglement swaps, we propose a novel adaptive quantum error correction (QEC) scheme that boosts end-to-end metrics. Specifically, depending on the network operating point, we adapt the code used in distillation over successive rounds to monotonically increase the rate while also improving fidelity. We demonstrate the effectiveness of this strategy using three codes, with parameters $[[9, 1, 3]]$, $[[9, 2, 3]]$, $[[9, 3, 3]]$, and a new performance metric, *efficiency*, that incorporates both overall rate and fidelity. Since the minimum input fidelity for QEC-based distillation is high, we then extend our study to include non-QEC-based purification protocols, specifically DEJMPS since it outperforms others. We compare the performance of end-to-end DEJMPS against adapting from DEJMPS to QEC once DEJMPS improves the initial fidelity to the threshold for QEC. Through a refined efficiency metric, we illuminate the regime where QEC is beneficial. These results provide a detailed outlook for entanglement purification and distillation in first and second generation quantum repeaters.

Index Terms—Quantum repeaters, entanglement distillation, stabilizer code, depolarizing channel, Werner state, DEJMPS

I. INTRODUCTION

QUANTUM networks fundamentally differ from classical networks since they rely upon entanglement distribution across the network nodes. Since direct transmission of quantum information across long distances suffers from an exponential scaling of loss [1], quantum repeaters are critical for wide area quantum networks. A repeater generates entanglement across single hops – short links with its neighboring nodes, which could be end-users or other repeaters – and performs entanglement swaps to create longer-range entanglement across longer hops. Since each link introduces loss, and swaps involve local operations that are noisy, *entanglement distillation* is used to distill fewer high fidelity entangled states from many noisy entangled states. Such distillation can be performed on single hops as well as longer hops, as long as classical communication is available across those hops. When end-users place requests for entanglement, the network must execute a mechanism to deliver entanglement at the necessary rate and fidelity, besides other metrics such as latency. This must be done through a combination of good entanglement generation, efficient distillation and smart routing protocols.

Hence, it is essential to develop scalable strategies for these processes that can meet the needs of different applications.

In this paper, we focus specifically on entanglement distillation across single and multiple hops. Entanglement can be distilled using local operations and classical communication (LOCC), which can be one- or two-way [2]. Classic 2-to-1 protocols require the nodes to perform two-way LOCC whereas protocols based on quantum error correction (QEC) only require one-way LOCC, significantly improving efficiency and reducing latency at the cost of increased complexity of LO. We consider QEC-based distillation protocols for second-generation quantum repeaters, where heralded entanglement generation addresses photon loss and QEC is used to correct errors introduced during LO [3]. Since recent years have witnessed an exciting amount of experimental demonstrations of QEC in different hardware technologies [4]–[10], these protocols could indeed be implemented in the next few years. Our goal here is to demonstrate a novel approach to *adaptively* improve end-to-end metrics that combine both rate and fidelity. Hence, to highlight the key insights and keep the setup simple, we incorporate noise in the initial generation of Bell pairs but assume that all other components are noiseless. In principle, memory decoherence or noise in LO can be mapped back to the initial fidelity of the Bell pairs, potentially with some Pauli twirling. We emphasize that our innovation can be adapted to realistic noise settings with careful considerations of decoherence and fault tolerance. Since these considerations will distract from the central focus of this work, and warrant an independent investigation on their own, we leave them for subsequent follow-up work.

We consider a linear chain of odd number of repeaters where each repeater generates entanglement with its neighboring nodes, distills, and then swaps them. The process continues until the end nodes have shared Bell pairs that they have distilled themselves. But independent of the length of the chain, we set the maximum number of distillation rounds to 3, as explained later. The entanglement generation is deterministic but the created state is a *Werner state*, where the Werner parameter could be interpreted as incorporating decoherence as well as noise in LO. These are the minimal assumptions we need to demonstrate our adaptive protocol. Conventional schemes apply the same distillation, or purification, procedure in each round to generate end-to-end entanglement of desired fidelity. However, we start with an $[[n, k, d]]$ stabilizer code, C_1 , with low rate, $R = \frac{k}{n}$, to correct many errors and improve the fidelity after the first round of distillation at single hops. After swapping the resulting k Bell pairs, we adaptively switch to a different $[[n, k' > k, d']]$ code, C_2 , that is able to further improve the fidelity while having a higher rate $R' = \frac{k'}{n} > R$. This is done carefully only when the input fidelity to the first round is just large enough to ensure that the resulting (output)

The authors are with the Department of Electrical and Computer Engineering, University of Arizona, Tucson AZ 85721. E-mail: { sijiecheng , narayananr }@arizona.edu

fidelity is above the input fidelity threshold for the second code. For the third round of distillation, we adapt once again by picking yet another $[[n, k'' > k', d''']]$ code, C_3 , if the channel operating point, i.e., depolarizing rate, is suitable. We fix n throughout so that LO need not change greatly.

For illustration of the idea, our simulations are conducted using the following codes: $C_1 : [[9, 1, 3]]$, $C_2 : [[9, 2, 3]]$, $C_3 : [[9, 3, 3]]$. We compare four protocols, $\mathcal{P}_1 : C_1 - C_1 - C_1$, $\mathcal{P}_2 : C_1 - C_2 - C_2$, $\mathcal{P}_3 : C_1 - C_2 - C_3$, and $\mathcal{P}_4 : C_2 - C_2 - C_2$, and show the regions where each one is advantageous. Our metric for comparison is a combination of overall rate (not just the code rate) and fidelity, which we call *efficiency*. Such adaptive QEC for entanglement distillation in quantum repeaters is unprecedented and opens up exciting new ways to achieve end-to-end metrics of quantum network applications. These can be adapted for more realistic noise settings and the advantages will still qualitatively hold, but for a more sophisticated definition of network operating point. We leave those deep investigations, e.g., a general construction of code sequences as a function of target metrics, their fault tolerance requirements, and resource estimates, for future work.

In the above exploration of adaptive QEC, the minimum required input fidelities for the codes are high, $\gtrsim 90\%$. For near-term implementation, it is important to keep the codes small but plan for low input fidelities, $\approx 70 - 80\%$, especially while accounting for decoherence and noise in LO. Even in the long-term, the fault-tolerant thresholds for large quantum low-density parity-check (QLDPC) codes are also expected to be high. Hence, we consider the use of classic non-QEC-based entanglement purification protocols such as BBPSSW [11] and DEJMPS [12] to improve initial fidelities to the threshold of the above QEC codes¹. We first show that DEJMPS with no twirling comprehensively outperforms BBPSSW (with/without twirling), so we restrict our consideration to only DEJMPS for the rest of the paper. We illuminate the asymmetric nature of the Pauli error probabilities for DEJMPS and show that it enables the protocol to rapidly improve fidelities in each round. Then we use DEJMPS to improve initial fidelities to the threshold of the $[[9, 3, 3]]$ code, chosen for its high rate compared to the other two codes. We highlight the emergence of ‘‘checkpoints’’ in the input-output fidelity plot as the minimum required number of DEJMPS rounds decreases with increasing input fidelity. After DEJMPS improves the input fidelity above the code threshold, we consider switching to one round of the QEC protocol and compare it to continuing with further DEJMPS rounds to achieve the same performance. We refine our previously defined efficiency metric to account for the subtleties of this setting. Using this refined metric, we highlight the regions where pure DEJMPS outperforms the switch to QEC and vice-versa. Importantly, we observe that it is the high rate of the QEC code that provides an edge at very high input fidelities, rather than the output fidelity.

This suggests that the design of second generation repeaters must carefully inspect the choice and value of a QEC code to replace or co-exist with simpler protocols such as DEJMPS.

¹Note that in the QEC literature this is called a ‘pseudo-threshold’ since it is for a specific code and not a property of a family of codes. A ‘threshold’ usually refers to a family. Here, we will use ‘threshold’ for convenience.

We expect that QEC would become a preferable choice under a fault-tolerant setting, but the details of the code and protocol will be critical to ensure superior performance to DEJMPS. We are not aware of prior works that have closely examined the evolution from first- to second-generation repeaters, so we think that our initial investigation will lead to many more careful studies of this important technological aspect.

The paper is organized as follows. Section II introduces the necessary technical background, Section III discusses our adaptive protocol, Section IV demonstrates the simulation results for our protocol, Section V explores the extension to non-QEC-based protocols, and Section VI concludes the paper by exploring avenues for future work. Appendix I provides analytical details of the comparison between BBPSSW and DEJMPS in Section V.

II. BACKGROUND

To better understand the ideas we propose, let us first recall the fundamental concepts and unify the notation used throughout this paper.

A. Stabilizer Formalism

A *stabilizer group*, \mathcal{S} , is a set of commuting Hermitian Pauli operators that does not contain $-I$. The commutativity implies that these operators can be simultaneously diagonalized. Since their eigenvalues are ± 1 , there exist a subspace of quantum states that are $+1$ -eigenvectors of all stabilizers. This subspace is referred to as a *stabilizer code*, $\mathcal{C}(\mathcal{S})$. For example, consider a 3-qubit stabilizer group generated by two operators: $S_1 = ZZI, S_2 = IZZ$. A quantum state $|\psi\rangle$ is in the stabilizer code if $S_1|\psi\rangle = |\psi\rangle, S_2|\psi\rangle = |\psi\rangle$. In this case it can be checked that the state takes the form $|\psi\rangle = \alpha|0\rangle + \beta|1\rangle$, where $\alpha, \beta \in \mathbb{C}$ satisfy $|\alpha|^2 + |\beta|^2 = 1$. The logical Pauli operators for the code are those that commute with every stabilizer but do not belong to \mathcal{S} themselves. The weight of a Pauli operator is given by the number of qubits on which it is not the identity, e.g., ZZI has weight 2. If there are $m = n - k$ independent stabilizers on n qubits, and the minimum weight of a logical operator is d , then the code has parameters $[[n, k, d]]$. The above example gives a $[[3, 1, 1]]$ code since $ZII \equiv IZI \equiv IIZ$ is a logical operator. This formalism simplifies the analysis of quantum error correction and is widely used for code design.

For the purposes of this paper, we will consider the distillation of the standard Bell state $|\Phi^+\rangle = \frac{1}{\sqrt{2}}(|00\rangle + |11\rangle)$. This state forms the one-dimensional $+1$ -eigenspace of the stabilizer group $\mathcal{S}_{++} = \langle +XX, +ZZ \rangle$. The other Bell states $|\Phi^-\rangle = \frac{1}{\sqrt{2}}(|00\rangle - |11\rangle), |\Psi^\pm\rangle = \frac{1}{\sqrt{2}}(|01\rangle \pm |10\rangle)$ correspond to the stabilizer groups $\mathcal{S}_{-+} = \langle -XX, ZZ \rangle, \mathcal{S}_{+-} = \langle \pm XX, -ZZ \rangle$. These states can be thought of as the standard Bell state with a Pauli error XI, ZI, YI .

B. Error Syndromes

Errors in a quantum system can be detected using the stabilizer formalism by measuring error syndromes. When an error E acts on a code state $|\psi\rangle$, it may commute or anti-commute with stabilizer operators S_i :

$$E|\psi\rangle = ES_i|\psi\rangle = \pm S_i E|\psi\rangle = \lambda_i S_i(E|\psi\rangle). \quad (1)$$

This means that measuring the stabilizer will give an eigenvalue of $\lambda_i = \pm 1$, where -1 s indicate the presence of an error. The error syndrome is a binary vector that records these eigenvalues: $\mathbf{s} = (\lambda_1, \lambda_2, \dots, \lambda_m)$. For example, consider an error $E = XII$ acting on the $[[3, 1, 1]]$ code defined earlier. We calculate the syndrome as follows:

$$\begin{aligned} ES_1 |\psi\rangle &= XII \cdot ZZI |\psi\rangle = -ZZI \cdot XII |\psi\rangle = -S_1 E |\psi\rangle, \\ ES_2 |\psi\rangle &= XII \cdot IZZ |\psi\rangle = IZZ \cdot XII |\psi\rangle = +S_2 E |\psi\rangle. \end{aligned}$$

Thus, the syndrome for this error is: $\mathbf{s} = (-1, +1)$. By measuring the stabilizers, we obtain the syndrome \mathbf{s} , which helps identify which error has occurred. Decoding algorithms use the syndrome to determine and correct the error, restoring the original quantum state if there are not too many errors.

C. Depolarizing Noise Channel

The depolarizing noise channel is a fundamental noise model in quantum information theory. It describes the effect of a qubit undergoing a random Pauli error with a certain probability. For a single-qubit state ρ , it is defined as:

$$\mathcal{E}_p(\rho) = (1-p)\rho + \frac{p}{3}(X\rho X + Y\rho Y + Z\rho Z), \quad (2)$$

where p is the depolarizing probability. This means that with probability $1-p$, the qubit remains unchanged, and with probability $\frac{p}{3}$, one of the three Pauli errors X, Y, Z is applied.

In quantum communication, depolarizing noise reduces entanglement fidelity by introducing errors in transmitted qubits. Specifically, when applied to Bell states, depolarizing noise transforms a perfect Bell state $|\Phi^+\rangle$ into a Werner state, a mixed state that retains some entanglement but requires purification for reliable quantum applications.

D. Werner States

A Werner state is a specific type of mixed state obtained when a Bell state is subject to depolarizing noise. Applying the depolarizing channel to $|\Phi^+\rangle$, we obtain:

$$\rho_W = W|\Phi^+\rangle\langle\Phi^+| + (1-W)\frac{I}{4}. \quad (3)$$

Since the identity can be decomposed into Bell states, i.e.,

$$I = |\Phi^+\rangle\langle\Phi^+| + |\Phi^-\rangle\langle\Phi^-| + |\Psi^+\rangle\langle\Psi^+| + |\Psi^-\rangle\langle\Psi^-|, \quad (4)$$

we rewrite ρ_W as:

$$\begin{aligned} \rho_W &= \left(W + \frac{1}{4}(1-W)\right) |\Phi^+\rangle\langle\Phi^+| \\ &+ \frac{1}{4}(1-W) (|\Phi^-\rangle\langle\Phi^-| + |\Psi^+\rangle\langle\Psi^+| + |\Psi^-\rangle\langle\Psi^-|) \\ &= \frac{3W+1}{4} |\Phi^+\rangle\langle\Phi^+| \\ &+ \frac{1}{4}(1-W) (|\Phi^-\rangle\langle\Phi^-| + |\Psi^+\rangle\langle\Psi^+| + |\Psi^-\rangle\langle\Psi^-|). \end{aligned} \quad (5)$$

By defining Fidelity F as $F = \frac{3W+1}{4} \Rightarrow W = \frac{4F-1}{3}$, we express ρ_W in terms of fidelity:

$$\begin{aligned} \rho_W &= F|\Phi^+\rangle\langle\Phi^+| \\ &+ \frac{1-F}{3} (|\Phi^-\rangle\langle\Phi^-| + |\Psi^+\rangle\langle\Psi^+| + |\Psi^-\rangle\langle\Psi^-|). \end{aligned} \quad (6)$$

E. Distillable Entanglement

The efficiency of one-way hashing method is determined by the number of distilled ideal Bell pairs, m , from n pairs of qubits each in a Werner state, given by:

$$D_H = \frac{m}{n} = 1 - S(W), \quad (7)$$

where $S(W)$ is the von Neumann entropy of ρ_W :

$$S(W) = -F \log_2 F - (1-F) \log_2 \left(\frac{1-F}{3}\right). \quad (8)$$

For a Werner state with fidelity F , the distillable entanglement obtained using one-way hashing is [13]:

$$\begin{aligned} D_H &= 1 - S(W) \\ &= 1 + F \log_2 F + (1-F) \log_2 \left(\frac{1-F}{3}\right). \end{aligned} \quad (9)$$

This method is effective when $F > 0.81071$, i.e., $D_H > 0$.

When we have three nodes, let W_1 be the parameter between nodes 1 and 2, and W_2 be the parameter between nodes 2 and 3. Then, after a swap at node 2, we have the effective Werner parameter between nodes 1 and 3,

$$\begin{aligned} W_{\text{eff}} &= W_1 W_2 \\ &= \left(\frac{4F_1-1}{3}\right) \left(\frac{4F_2-1}{3}\right), \end{aligned} \quad (11)$$

$$\begin{aligned} F_{\text{eff}} &= \frac{1}{4} + \frac{3}{4} W_{\text{eff}} \\ &= \frac{1}{4} + \frac{3}{4} \left(\frac{4F_1-1}{3}\right) \left(\frac{4F_2-1}{3}\right). \end{aligned} \quad (12)$$

When we have n nodes, we will have W_1, \dots, W_{n+1} , so

$$F_{\text{eff}} = \frac{1}{4} + \frac{3}{4} \prod_{i=1}^{n+1} \left(\frac{4F_i-1}{3}\right). \quad (13)$$

For successful distillation, the threshold condition is:

$$\prod_{i=1}^{n+1} \left(\frac{4F_i-1}{3}\right) > 0.747613. \quad (14)$$

F. Distillation based on Error Correction

The protocol begins with n Bell States shared between Alice and Bob. Instead of sending them directly, Alice projects these states to the subspace of a stabilizer code. Since we use Bell states, the encoding can be implemented via stabilizer measurements on the initial Bell pairs. After encoding, Alice obtains k encoded Bell pairs along with a set of stabilizers. The process is as follows [14], [15]:

- 1) **Encoding:** Alice performs stabilizer measurements on the Bell states to obtain coded Bell pairs.
- 2) **Classical Communication:** Alice sends the stabilizer generators and measurement outcomes (syndromes) to Bob through a classical channel.
- 3) **Noisy Transmission:** Alice transmits one half of the coded Bell pairs to Bob through a noisy quantum channel while keeping the other half.

- 4) **Error Detection:** Upon receiving the transmitted part, Bob applies stabilizer-based syndrome measurements using the same stabilizer generators to detect errors introduced by the channel and obtain the detected syndromes.
- 5) **Error Correction:** Using the stabilizer generators, the syndrome received from Alice, and the detected syndrome, Bob applies decoding to estimate the error and correct it using quantum gates.

If the estimated error matches the actual error, up to stabilizers, then Bob successfully corrects it, restoring the encoded Bell pairs to a perfect state. After successful error correction, Alice and Bob share a set of perfectly encoded Bell pairs, enabling robust long-distance quantum communication.

G. Protocol Rate

In this paper, the protocol rate refers to the ratio of the total number of entanglement links finally established from Alice to Bob and the total number of entangled states consumed throughout the protocol. For a multi-repeater setup, entanglement is generated at each segment of the communication link, potentially distilled, and then swapped. We define:

- n_{in} as the total number of Bell pairs required across all links in the network.
- n_{out} as the final number of successfully shared high-fidelity Bell pairs between Alice and Bob.

Thus, the protocol rate is given by:

$$R = \frac{n_{\text{out}}}{n_{\text{in}}}. \quad (15)$$

A higher protocol rate indicates a more efficient high-fidelity entanglement distribution process. Later, we will define an efficiency metric that combines this rate with fidelity.

III. ADAPTIVE ERROR CORRECTION PROTOCOL

A. Stabilizer Codes

In this work, we obtain stabilizer codes from the *CodeTables* database [16] and then transform them into standard form as outlined in [17, Chapter 10]. We describe the codes in the form of matrices whose entries are Pauli operators. Each row of the stabilizer matrix H (resp. logical operator matrix \bar{X} or \bar{Z}) corresponds to an independent stabilizer (resp. logical X or logical Z) of the code. To illustrate the main ideas, we focus on the $[[9, 1, 3]]$, $[[9, 2, 3]]$ and $[[9, 3, 3]]$ codes shown in Table I. As an initial test for uncovering structural properties relevant to distillation, we also examine the well-known $[[5, 1, 3]]$ and $[[7, 1, 3]]$ codes. However, we emphasize that our method can be suitably adapted to other sequences of stabilizer codes.

B. Decoder Based on Lookup Table

The lookup table decoder is a method for quantum error correction that maps syndromes to error patterns using a precomputed table. It operates with the following steps:

- 1) **Syndrome Measurement:** The stabilizer measurements yield an error syndrome, $\mathbf{s} = (\lambda_1, \lambda_2, \dots, \lambda_m) \in \{\pm 1\}^m$.
- 2) **Error Identification via Lookup Table:** The syndrome is matched with a stored minimum-weight error in the

$[[9, 1, 3]]$	$[[9, 2, 3]]$	$[[9, 3, 3]]$
$H = \begin{bmatrix} YZIIIIIXY \\ ZYIIIIIXX \\ ZZYIIIIIXI \\ IIIIXIIIII \\ IIIIXIIIII \\ IIIIXIIIII \\ IIIIXIIIII \\ IIIIXIIIII \\ IIIIXIIIII \\ IZZIIIIIZZ \end{bmatrix}$	$H = \begin{bmatrix} YZZZIIIXII \\ ZYZIZIXYY \\ ZIYZIIXYX \\ ZIIXIIIIY \\ IIZIYIIXI \\ IIIIXIIIII \\ IZZZZIIZZ \end{bmatrix}$	$H = \begin{bmatrix} YZIZIIXYX \\ IXZZIXYIY \\ ZIYZIIXYX \\ IZIYIIXYZ \\ IIIIXIIIII \\ ZZZZIZZZZ \end{bmatrix}$
$\bar{X} = [ZIIIIIIIXX]$	$\bar{X} = \begin{bmatrix} IZZIIIXXI \\ IZIZIIXIX \end{bmatrix}$	$\bar{X} = \begin{bmatrix} ZZIIIXXII \\ IIZZIXIXI \\ IZIZIIXIX \end{bmatrix}$
$\bar{Z} = [ZZIIIIIIIZ]$	$\bar{Z} = \begin{bmatrix} IZZIZIIZI \\ IZZIIIIIZ \end{bmatrix}$	$\bar{Z} = \begin{bmatrix} ZZIZIIZII \\ ZIZZIIIZI \\ ZZZIIIIIZ \end{bmatrix}$

TABLE I: The three 9-qubit codes that we use for simulations.

lookup table as the estimated error. This is the maximum likelihood decoding strategy for the depolarizing channel (i.e., Werner states).

- 3) **Error Correction:** If the estimated error exactly matches the actual error, up to a stabilizer, then decoding is successful. Otherwise, logical operators are used to check which logical qubits are in error.

For $k = 1$ logical qubit, the logical error rate is the same as the per-logical-qubit error rate. However, for $k > 1$ logical qubits, each logical qubit can suffer from different logical error rates. In our results, a lower-bound strategy is used (for output fidelity): the logical error rate for each qubit is taken to be the overall logical error rate of the code. This method provides an efficient way to handle errors in small-distance quantum codes and can be used for practical quantum networking applications.

C. Number of Distillation Rounds

We want to determine a scalable structure for a chain of repeaters based on several rounds of distillation and entanglement swaps to increase the output fidelity.

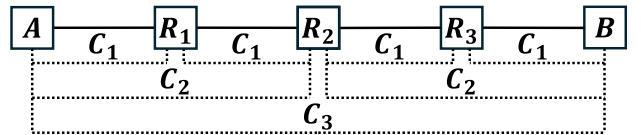


Fig. 1: Protocol diagram for three repeaters.

To determine the optimal number of distillation rounds, the three-repeater situation provides a suitable case for analysis. To clarify, let's start with a three-repeater configuration, with the structure shown in Fig. 1. This setup includes Alice, a chain of repeaters from R1 to R3, and Bob.

First, entanglement links are established between the following adjacent pairs: Alice and R1, R1 and R2, R2 and R3, and R3 and Bob. Next, entanglement distillation is performed independently for each link using code C_1 . Then, quantum swaps are performed to generate entanglement links between Alice and R2, and between R2 and Bob.

Subsequently, distillation is applied using code C_2 between Alice and R2, and between R2 and Bob. In this process, distillation is always performed between the two nodes closest to the current entanglement link. Next, a final quantum swap

is performed to establish an entanglement link between Alice and Bob. Finally, end-to-end distillation is carried out between Alice and Bob using code C_3 .

In the first test experiment, we want to start with something simple. So, we use these two codes: $[[5, 1, 3]]$ and $[[7, 1, 3]]$, which are well known for encoding a single logical qubit, but one has a lower rate than the other.

In Fig. 2, the title of each subfigure follows the format “C-X-X”, where “C” indicates that distillation is performed in that round using either code, and “X” means that distillation is not performed in the corresponding round. Legends beginning with “OR” indicate cases without repeaters (i.e., these are just logical error rates for the codes). For example:

(a) represents performing only the first round of distillation. “OR, $[[5, 1, 3]]$ ” and “OR, $[[7, 1, 3]]$ ” denote directly establishing the entanglement link between Alice and Bob without repeaters, using the $[[5, 1, 3]]$ and $[[7, 1, 3]]$ codes, respectively. These curves are simply the logical error rates of the codes, plotted as input fidelity vs output fidelity. In this context, “ $[[5, 1, 3]]$ -X-X” indicates that only the first round of distillation is performed, using the $[[5, 1, 3]]$ code.

(b) refers to performing the first and second rounds.

(c) refers to performing the first and third rounds.

(d) refers to performing all three rounds.

Since, based on our assumption, the depolarizing noise originates from the first round of distillation, the first round is the most important. The final end-to-end round of distillation is also important because it can fix errors generated during intermediate swaps, which makes it the second most important. Comparing Fig. 2b and Fig. 2c, both apply the first round, but one includes the second and the other includes the final. As shown in the plots, Fig. 2b performs better, suggesting that having only the first and final rounds may not be enough.

Comparing Fig. 2a, Fig. 2b and Fig. 2d, we find that as the number of rounds increases, the last-performed round in each configuration contributes the least benefit. So the second round ranks third in importance. This suggests that adding more rounds of distillation in the middle provides diminishing benefits as the number of rounds increases, potentially leading to a decrease in the link-building speed. Therefore, it is reasonable to limit the number of distillation rounds to three.

D. Simulation Setup

Given that we fix the number of distillation rounds to three, this strategy can be extended to configurations with any number of repeaters. To clarify, let’s start with a single repeater, with the structure shown in Fig. 3. This means we have Alice, the repeater, and Bob. First, Alice and the repeater, as well as the repeater and Bob, will each generate an entanglement link. Next, they will perform distillation by using code C_1 separately. Then, we will perform a quantum swap to generate the entanglement link between Alice and Bob. Afterward, we will conduct distillation by using code C_2 between Alice and Bob. In this process, we aim to perform distillation between the two nodes that are closest to the current distillation. Finally, an end-to-end distillation by using code C_3 will be performed between Alice and Bob. In this specific situation, we will

perform distillation between Alice and Bob twice to align with our three-round distillation strategy.

A more general case is shown in Fig. 4 for the setting of five repeaters, still with three rounds of distillation.

E. Assumptions

For our error correction-based distillation model, we use distillable entanglement as part of the end-to-end metric. To simplify the model, we assume that the only source of noise is the depolarizing channel, while all other components are ideal. This means that whenever we attempt to generate entanglement between two nodes, it will always succeed with 100% probability, and there is no loss in the channel. Our primary goal here is to demonstrate the effectiveness of our adaptive distillation protocol in the simplest nontrivial setting.

We assume that the distance and circumstances between each pair of nodes are identical, meaning they will have the same input fidelity. Therefore, we can use a single input fidelity value to represent the fidelity between all adjacent nodes. Thus, we define this input fidelity as our F_{in} .

The generated Bell pairs are considered ideal, and we simplify the noise model by assuming twirling is applied to produce depolarized Bell pairs. Quantum memories are assumed to hold qubits indefinitely without any decoherence or loss. Note that they only need to hold qubits until they are consumed in the next swap or distillation, which will not be very long. Additionally, distillation and swapping operations are treated as ideal, with no errors. If we consider circuit-level errors, then the entire scheme must be made fault-tolerant for our sequence of codes, which warrants an entire paper for itself that considers all the subtle details. We do intend to perform that analysis as a natural follow-up to this work.

F. Introduction to the Algorithm

Our simulation setup is built on MATLAB. When we try to build our algorithm, there are two major issues that need to be solved. The first one is the noise generation problem. When generating random Pauli noise, we expect it to be truly random. As is well-known, random numbers generated by modern classical computers are all pseudo-random. Thus, generating results that approximate true randomness correctly is a significant goal for our algorithm. The second issue arises from the fact that the final result represents a probability distribution, which means we need a large number of noise simulations to obtain reliable final results. Based on our experiments, each mapping point between input fidelity F_{in} and output fidelity F_{out} requires at least 1,000,000 simulations to obtain a relatively accurate result. As a result, accelerating this process becomes the core goal of the algorithm.

To address these issues, we propose an algorithm which uses a fixed probability to replace random error generation.

1) *Part I: Constructing the Logical Error Rates (OR)*: First, as shown in Fig. 5, we need to construct the F_{in} - F_{out} map for the 0-Repeater case, which will serve as a reference for subsequent parts. When multiple repeaters are introduced, if the input noise is depolarizing, then after performing a quantum swap, the resulting noise remains depolarizing. Therefore,

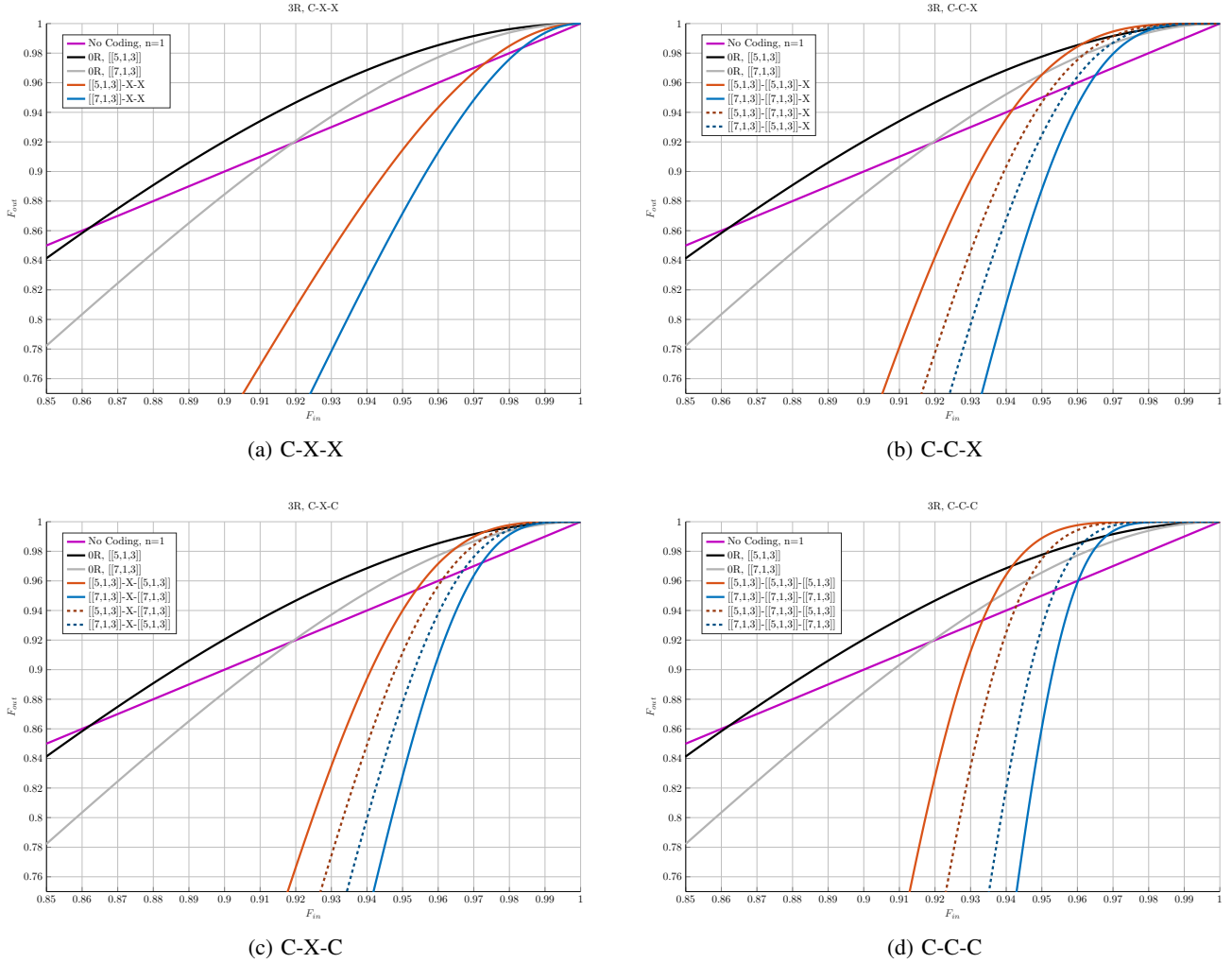


Fig. 2: Three Rounds of Distillation. Legend entry “No Coding” means $F_{\text{out}} = F_{\text{in}}$, that is, no coding is used.

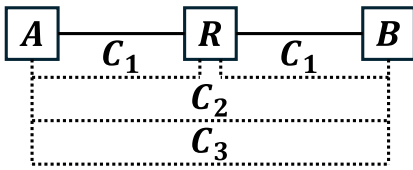


Fig. 3: Protocol diagram for a single repeater, where we still perform three rounds of distillation.

when performing error correction in the next round, we can directly use the $F_{\text{in}}-F_{\text{out}}$ map from the 0-Repeater case to determine F_{out} after the next round of error correction, thereby accelerating the simulation process.

Step 1: Construct the F_{in} Sequence:

In this step, we uniformly select 1000 points from $F_{\text{in}} = 0$ to $F_{\text{in}} = 1$. At the same time, we generate the probabilities P_X , P_Y , and P_Z based on the characteristics of depolarizing noise.

Step 2: Construct the All Error List:

We list all possible error events (including the case where no error occurs) and sort them in ascending

order based on their error weight. That is, the first error in the list is the most probable error, the second error is the second most probable one, and so on. If we describe the error-correcting code using $[[n, k, d]]$, then the total number of possible error combinations based on the syndrome is $2^{(n-k)}$.

Step 3: Write Data into the All-Error List:

In this step, we need to perform three tasks. Using the points obtained from *Step 1*, calculate the probability of each error combination (for each of the 1000 selected points) and write this into the all-error list. Then, construct the Lookup Table and obtain the logical error based on the logical operator, then write it into the all-error list.

Step 4: Construct the Lookup Table:

This step is performed simultaneously with *Step 3*. For each processed error combination, we obtain its corresponding syndrome. If this syndrome has not been recorded in the Lookup Table, we record the error combination that triggers this syndrome. If the syndrome has already been recorded, it means that the current error combination is not the smallest-

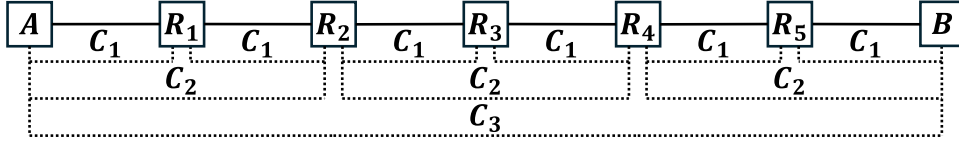


Fig. 4: Protocol diagram for five repeaters, where we perform only three rounds of distillation.

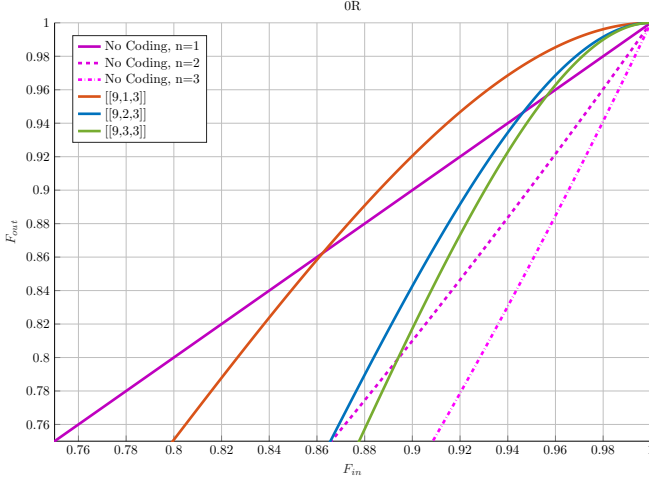


Fig. 5: The $F_{\text{in}}-F_{\text{out}}$ map for the 0-repeater case. As an example, the plot in the $F_{\text{in}}-F_{\text{out}}$ map is shown for $[[9, 1, 3]]$, $[[9, 2, 3]]$ and $[[9, 3, 3]]$. Additionally, the no-coding error rates for $n = 1$, $n = 2$ and $n = 3$ are provided as references.

weight error and does not need to be recorded, because in *Step 2*, we have already sorted the errors by weight.

Step 5: Obtain the Logical Error Corresponding to Each Error Combination:

This step is performed simultaneously with *Step 3*. After *Step 4*, we use the logical operator to determine the logical error caused by the current error combination. Then, we retrieve the smallest weight error from the Lookup Table corresponding to this syndrome and test whether it can accurately predict the logical error caused by the current error combination: If it can predict correctly, record it as correctable by the Lookup Table. Otherwise, record it as uncorrectable. Finally, write the results into the error list.

Step 6: Generate the $F_{\text{in}}-F_{\text{out}}$ Map:

From the all-error list, read all correctable logical error probabilities and accumulate them for each of the 1000 points (generated in *Step 1*). In the end, we obtain the $F_{\text{in}}-F_{\text{out}}$ map for 1000 points spanning $F_{\text{in}} = 0$ to $F_{\text{in}} = 1$.

2) *Part II: Constructing the Many-Repeater Situation:*

Before proceeding to this part, we need to repeatedly execute *Part I* to obtain all required $F_{\text{in}}-F_{\text{out}}$ maps for the error-correcting codes being used.

Step 1: Construct the F_{in} sequence:

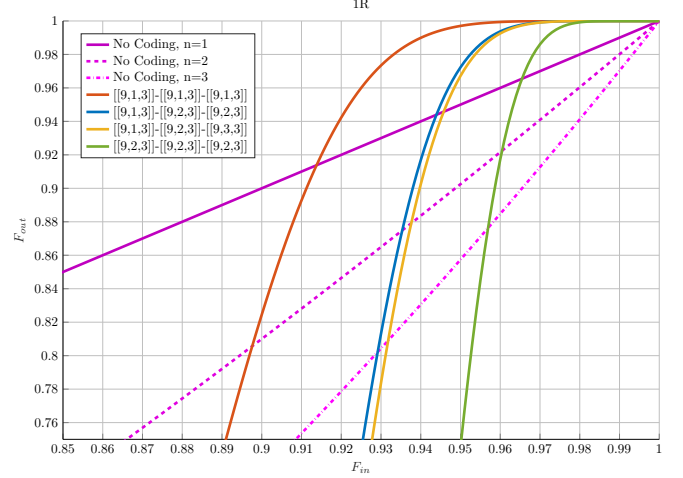


Fig. 6: the $F_{\text{in}}-F_{\text{out}}$ map for the 1-repeater case. This figure only shows the relationship between input fidelity and output fidelity based on different protocols. No coding means that no error-correcting code is used. For example, when $n = 1$, $F_{\text{out}}^{\text{No Coding}} = F_{\text{in}}$, which means that when the input is a single qubit, the output fidelity corresponds to the $n = 1$ qubit case. In general, $F_{\text{out}}^{\text{No Coding}} = F_{\text{in}}^n$.

In this step, we uniformly select a required number of points from $F_{\text{in}} = 0$ to $F_{\text{in}} = 1$ as needed.

Step 2: Perform error correction in this round:

Based on the F_{in} points constructed in *Step 1* and the chosen $[[n, k, d]]$ error-correcting code, we use `interp1()` to look up the corresponding $F_{\text{in}}-F_{\text{out}}$ map in 0-repeater case, where the F_{out} value represents the post-error-correction F_{out} at this round.

Step 3: Compute the output fidelity of entanglement swap: Based on our discussion in the background (Eqn. (12)), since in this case each round of error correction is based on the same codes, with the same input fidelity at the beginning, we can simplify the formula to the following form:

$$F_{\text{eff}} = \frac{1}{4} + \frac{3}{4} \left(\frac{4F_{\text{in}}-1}{3} \right)^{n_{\text{QS}}+1}$$
, where n_{QS} represents the total number of quantum swaps required in this round. The result obtained from this formula becomes the F_{in} for the next round.

Step 4: Obtain the final $F_{\text{in}}-F_{\text{out}}$ map:

By repeating *Step 2* and *Step 3* with different codes in each round, we complete error correction across all rounds and obtain the final $F_{\text{in}}-F_{\text{out}}$ map.

IV. SIMULATION RESULTS

A. Goal

Based on the single repeater situation, we can use various coding combinations. To describe this clearly, we will use the notation $\llbracket n_1, k_1, d_1 \rrbracket - \llbracket n_2, k_2, d_2 \rrbracket - \llbracket n_3, k_3, d_3 \rrbracket$ to represent the codes used at each round. For example, $\llbracket 9, 1, 3 \rrbracket - \llbracket 9, 2, 3 \rrbracket - \llbracket 9, 3, 3 \rrbracket$ means we will use $\llbracket 9, 1, 3 \rrbracket$ for the first round. To maintain system stability, we will use the same code for each link within the same round. Then, we will use $\llbracket 9, 2, 3 \rrbracket$ for the second round and $\llbracket 9, 3, 3 \rrbracket$ for the final end-to-end round. Here, we will compare $\llbracket 9, 1, 3 \rrbracket - \llbracket 9, 1, 3 \rrbracket - \llbracket 9, 1, 3 \rrbracket$, $\llbracket 9, 1, 3 \rrbracket - \llbracket 9, 2, 3 \rrbracket - \llbracket 9, 2, 3 \rrbracket$, $\llbracket 9, 1, 3 \rrbracket - \llbracket 9, 2, 3 \rrbracket - \llbracket 9, 3, 3 \rrbracket$ and $\llbracket 9, 2, 3 \rrbracket - \llbracket 9, 2, 3 \rrbracket - \llbracket 9, 2, 3 \rrbracket$.

To simplify our following description, let us define the notation for each protocol:

- Protocol₁: $\llbracket 9, 1, 3 \rrbracket - \llbracket 9, 1, 3 \rrbracket - \llbracket 9, 1, 3 \rrbracket$
- Protocol₂: $\llbracket 9, 1, 3 \rrbracket - \llbracket 9, 2, 3 \rrbracket - \llbracket 9, 2, 3 \rrbracket$
- Protocol₃: $\llbracket 9, 1, 3 \rrbracket - \llbracket 9, 2, 3 \rrbracket - \llbracket 9, 3, 3 \rrbracket$
- Protocol₄: $\llbracket 9, 2, 3 \rrbracket - \llbracket 9, 2, 3 \rrbracket - \llbracket 9, 2, 3 \rrbracket$

Because the number of outputs (i.e., logical qubits) is different across these codes, we will use the fidelity lower bound (see Section III-B) to describe the performance of each. This means that all output qubits being correct simultaneously is considered successful, while any single output qubit failure is considered a total failure. In practice, we wouldn't know which logical qubits are in error, so this is reasonable.

In Fig. 6, we observe that the choice of coding protocol can significantly affect the fidelity. We also observe that the logical qubit rate and distillable entanglement can be affected by different protocols. This implies that it is impossible to achieve an overall optimal result using a single code. Hence, our goal is to develop an adaptive strategy to switch between protocols at relatively optimal thresholds, balancing the trade-off between rate, fidelity, and distillable entanglement.

B. Efficiency Function

To demonstrate this multi-way tradeoff, we define the *efficiency function* as follows:

$$E(F_{\text{in}}) := \frac{n_{\text{out}} D(F_{\text{out}}(F_{\text{in}}))}{n_{\text{in}} D(F_{\text{in}})} = \frac{R_{\text{out}} D_{\text{out}}(F_{\text{in}})}{D(F_{\text{in}})}, \quad (16)$$

where:

- n_{in} is the number of entangled states consumed,
- n_{out} is the number of output entangled states,
- $R_{\text{out}} = \frac{n_{\text{out}}}{n_{\text{in}}}$ is the protocol rate,
- F_{in} is the input fidelity,
- $F_{\text{out}}(F_{\text{in}})$ is the output fidelity corresponding to F_{in} ,
- $D(F_{\text{in}})$ is the input distillable entanglement,
- $D_{\text{out}}(F_{\text{in}})$ is the output distillable entanglement.

To calculate the protocol rate, we must ensure that the number of output Bell pairs from the previous round matches the input required by the code used in the next round. Therefore, the rate must be calculated iteratively on a round-by-round basis.

1) *First Round Using the $\llbracket n_1, k_1, d_1 \rrbracket$ Code:* When discussing the first round, we need to consider the number of repeaters (n_R) to be used. The corresponding input and output qubits are shown below.

$$N_{\text{in}}^{(1)} = (n_R + 1) \cdot n_1 \quad (17)$$

$$K_{\text{out}}^{(1)} = k_1 \quad (18)$$

2) *Second Round Using the $\llbracket n_2, k_2, d_2 \rrbracket$ Code:* The key point in the second round is to match $K_{\text{out}}^{(1)}$ with n_2 . Therefore, we use $L^{(1)} = \text{lcm}(K_{\text{out}}^{(1)}, n_2)$. Thus, the corresponding input and output qubits are shown below.

$$N_{\text{in}}^{(2)} = \frac{L^{(1)}}{K_{\text{out}}^{(1)}} \cdot N_{\text{in}}^{(1)} \quad (19)$$

$$K_{\text{out}}^{(2)} = \frac{L^{(1)}}{n_2} \cdot k_2 \quad (20)$$

3) *Third Round Using the $\llbracket n_3, k_3, d_3 \rrbracket$ Code:* Similar to the second round, we need to use $L^{(2)} = \text{lcm}(K_{\text{out}}^{(2)}, n_3)$ to ensure proper matching between them. Thus, the final input and output qubits are shown below.

$$N_{\text{in}}^{(3)} = \frac{L^{(2)}}{K_{\text{out}}^{(2)}} \cdot N_{\text{in}}^{(2)} \quad (21)$$

$$K_{\text{out}}^{(3)} = \frac{L^{(2)}}{n_3} \cdot k_3 \quad (22)$$

Here, $N_{\text{in}}^{(3)}$ and $K_{\text{out}}^{(3)}$ are the total number of Bell pairs required for the input and the total number of output Bell pairs, respectively. Thus, we can set $n_{\text{in}} = N_{\text{in}}^{(3)}$ and $n_{\text{out}} = K_{\text{out}}^{(3)}$.

C. Results

1) *Single Repeater:* Based on our efficiency function, we choose the protocol with the maximum efficiency as the actual protocol to be used, depending on the input fidelity. Finally, we obtain the switching points as follows:

- From Protocol₁ to Protocol₂: $F_{\text{in}} = 0.9343$;
- From Protocol₂ to Protocol₃: $F_{\text{in}} = 0.9356$;
- From Protocol₃ to Protocol₄: $F_{\text{in}} = 0.9655$.

These switching points can be clearly observed in Fig. 7. The corresponding results for R_{out} , F_{out} and D_{out} are shown in Figs. 8.a, 8.b and 8.c, respectively.

2) *Multiple Repeaters:* Based on the discussion in the single-repeater scenario, we found that the critical part is identifying the switching point based on the efficiency function. According to our experiments, we found that for multiple repeaters, they behave similarly to the single-repeater scenario. However, as the number of repeaters increases, all optimal switching points move to the right, meaning that higher input fidelity is required as the trigger to switch between protocols and achieve optimal efficiency.

From Fig. 9, we can identify the switching points for the adaptive protocol on three repeaters as follows:

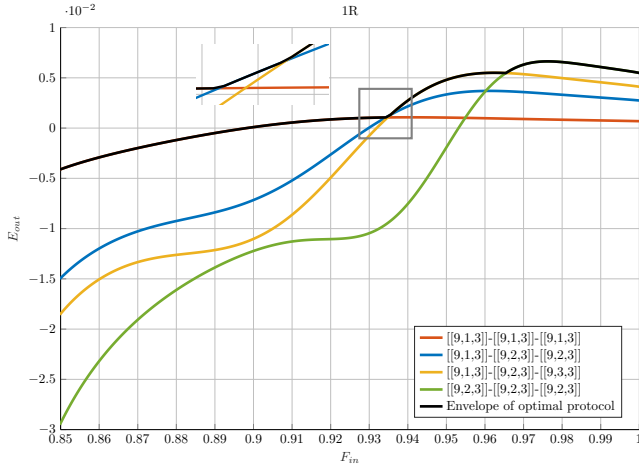
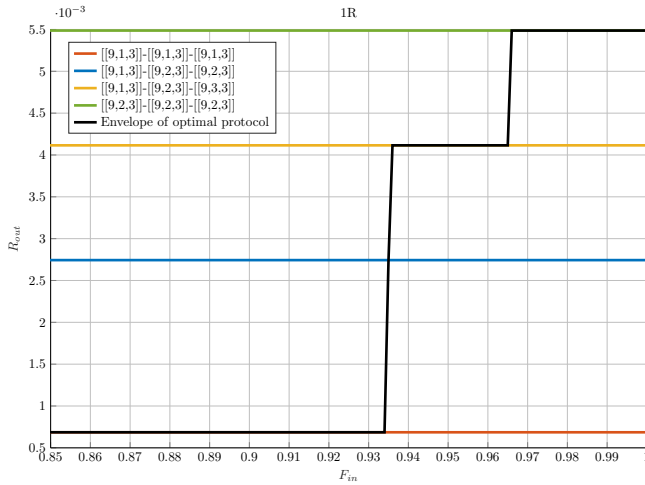


Fig. 7: The F_{in} - E_{out} map for the 1-repeater case with the envelope highlighting the optimal protocol. This figure shows the relationship between efficiency and input fidelity, using input fidelity as the reference for adaptive switching. We zoom in on the region where the switch occurs from Protocol₁ to Protocol₃. The reason we include Protocol₂, even though it is optimal only for a very short input fidelity range, is that we aim to minimize changes in k during each round. When switching between two closely spaced adaptive protocols, keeping k as stable as possible ensures smoother system performance, especially when noise varies continuously over time.



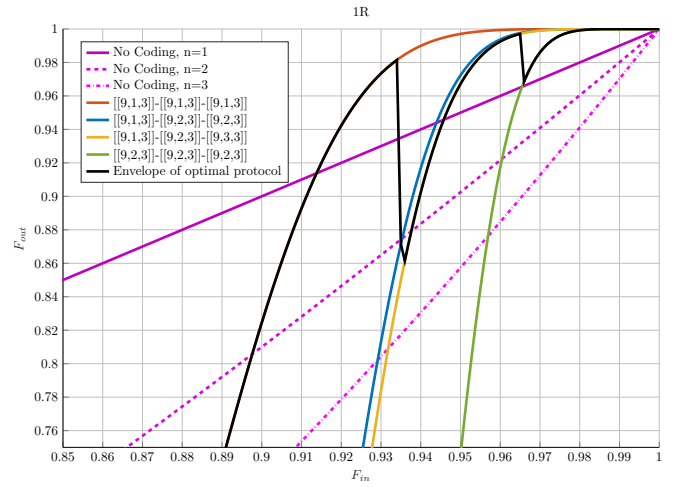
(8.a) The F_{in} - R_{out} map for the 1-repeater case with optimal envelope.

- From Protocol₁ to Protocol₂: $F_{in} = 0.9465$;
- From Protocol₂ to Protocol₃: $F_{in} = 0.9474$;
- From Protocol₃ to Protocol₄: $F_{in} = 0.9717$.

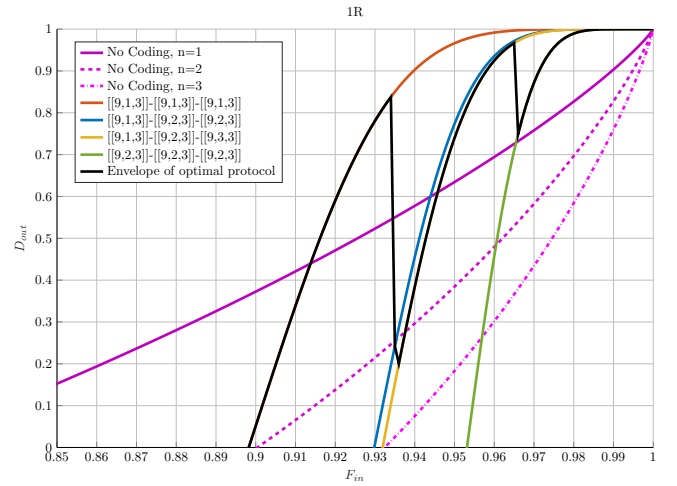
From Fig. 10, we can identify the switching points for the adaptive protocol on five repeaters as follows:

- From Protocol₁ to Protocol₂: $F_{in} = 0.9524$;
- From Protocol₂ to Protocol₃: $F_{in} = 0.9532$;
- From Protocol₃ to Protocol₄: $F_{in} = 0.9747$.

These have progressively increased from the single repeater and three repeaters cases. In Table II, we identify the switching points for different numbers of repeaters. We can easily see that the switching point increases with the number of repeaters.



(8.b) The F_{in} - F_{out} map for the 1-repeater case with optimal envelope.



(8.c) The F_{in} - D_{out} map for the 1-repeater case with optimal envelope.

Fig. 8: The 1-repeater case with optimal envelope. Based on the switching points from the efficiency function, we can observe an increase in the rate in Fig. 8.a as the input fidelity increases. In Fig. 8.b, we can see how the output fidelity changes as the input fidelity increases. In Fig. 8.c, we can see that distillable entanglement follows the same trend as fidelity. The general form of the “No Coding” plots is given by $D_{out}^{\text{No Coding}} = D_{out}(F_{in}^n)$.

#R	F_{SW}^1	F_{SW}^2	F_{SW}^3
1	0.9343	0.9356	0.9655
3	0.9465	0.9474	0.9717
5	0.9524	0.9532	0.9747
7	0.9561	0.9568	0.9766
9	0.9587	0.9594	0.9780
11	0.9608	0.9614	0.9791
13	0.9624	0.9630	0.9799
101	0.9779	0.9782	0.9881
1001	0.9877	0.9879	0.9934

TABLE II: The relationship between the switching points and the number of repeaters. #R represents the number of repeaters, and F_{SW}^n represents the switching points.

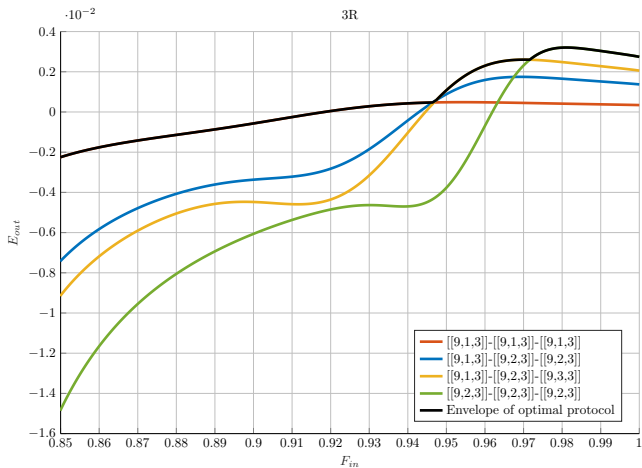


Fig. 9: The F_{in} - E_{out} map for three repeaters with optimal envelope. Observe that the protocol switching points moved to the right compared to the single repeater case.

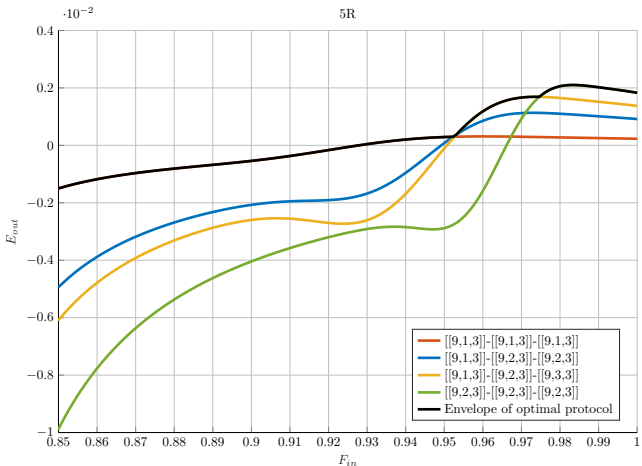


Fig. 10: The F_{in} - E_{out} map for five repeaters with optimal envelope. Observe that the protocol switching points moved to the right compared to the three-repeater case.

3) *General end-to-end metrics*: Our approach aims to show that by adaptively changing the code used for distillation in each round, we can achieve a higher value for the objective function compared to using a fixed code. We demonstrated this using the efficiency metric $E(F_{in})$. However, our key insight is that as long as the specific metric/objective function depends on both fidelity and rate, the adaptive approach should be advantageous. Even in the presence of realistic noise, an advantage should still be observed when dynamically adjusting the code/protocol depending on the network operating point.

V. EXTENDING ADAPTIVITY FROM 2G TO 1G ENTANGLEMENT PURIFICATION

All the discussions above are based on quantum error correction (QEC), and in general, we refer to this as the 2G protocol [3]. From the previous discussion, we can clearly see that the threshold is relatively high. If the input fidelity is lower

than this threshold, we may need to apply a 1G protocol [3] first to increase the input fidelity to the required threshold.

In Lorenzo et al. [18], entanglement distillation based on the DEJMPS is used to generate high-fidelity Bell pairs whose Pauli error probabilities can be strongly asymmetric. The distilled pairs are then interpreted as an effective Pauli teleportation channel, and this asymmetry is directly exploited by asymmetric quantum error correction codes. As a result, the required number of distillation rounds becomes a design parameter that must be optimized jointly with the chosen code, depending on the target reliability and the resource and latency constraints.

In our setting, we instead apply Werner twirling after DEJMPS (1G) to symmetrize the biased noise into an effective depolarizing model for 2G. This allows us to use a threshold-based criterion to specify the target fidelity or physical error rate required from DEJMPS, thereby providing a more transparent rule to select the number of distillation rounds. This also enables a cleaner efficiency metric that jointly accounts for distillable entanglement and the number of output qubits. In particular, when the input Bell pairs are affected by non-depolarizing noise, multiple rounds of DEJMPS do not necessarily preserve a consistent Z -biased structure. This makes it difficult to select or design a single bias-tailored quantum error correction code that is robust across general operating conditions. By contrast, our twirling based approach produces a uniform depolarizing description after distillation, which makes the overall design procedure easier to apply to a wide range of scenarios. In this paper, we use the depolarizing model as the main illustrative example for the input.

A. 1G Protocol

In 2G protocols, all Bell pairs are retained, and QEC is applied to improve their fidelity. While it is advantageous that all Bell pairs are preserved, the threshold for effective operation is quite high.

The 1G protocol is fundamentally different. In general, it begins by generating two Bell pairs, then measuring one of them and using the result to decide whether to keep the other. This means that at least around 45% of the Bell pairs are discarded in order to forcibly boost the output fidelity when the input fidelity is close to 0.5 in the first round. However, as the input fidelity increases, the discard rate decreases. As a result, the output fidelity can be significantly higher than that of 2G protocols, but this comes at the cost of losing many Bell pairs.

During the NISQ era, source Bell pairs are extremely precious, so using 1G protocols is not always the most practical choice. However, they serve as an effective approach to raise the input fidelity to the threshold required for 2G operation.

B. 1G Simulator

In general, the 1G protocol is based on a quantum circuit. To simulate it in a clear and systematic way, we use the stabilizer formalism to calculate all results step by step, gate by gate. Similar to the previous section, we also list all possible errors and calculate the probability of each one. However, the 1G

protocol exhibits a sharp transition at $F_{\text{in}} = 0.5$, making the $F_{\text{in}} - F_{\text{out}}$ mapping effectively step-like (discontinuous and piecewise constant). Therefore, using `interp1()` to densify the mapping (e.g., from 1,000 points to 10,000) is not valid globally: near this sharp jump, interpolation can produce non-physical intermediate values or become numerically unstable. In practice, interpolation may only be reliable when restricted to $F_{\text{in}} > 0.5 + \epsilon$ (with a small $\epsilon > 0$) and sufficiently far from the transition. For robustness across all input fidelities, we do not use `interp1()` for the 1G protocol. Instead, we must either generate the 1G protocol results in real time according to the protocol's sequence or precompute all required data points in advance. The process for generating the plots of the 1G purification protocols is summarized as follows:

Step 1: Set the required input:

Provide the complete protocol circuit and define the input state based on the stabilizer formalism. Then, specify several groups, each consisting of two qubits. Later, if the measurement results of any group do not match, its outcome will be marked as discarded. Finally, specify the number of rounds to be executed.

Step 2: Construct the F_{in} Sequence:

In this step, we uniformly select 10000 points from $F_{\text{in}} = 0$ to $F_{\text{in}} = 1$. At the same time, we generate the probabilities P_X , P_Y , and P_Z based on the characteristics of depolarizing channel or input by hand.

Step 3: Determine whether to apply twirling:

If the protocol requires twirling in each round, this step redistributes the errors according to the depolarizing model. Otherwise, the probabilities of P_I , P_X , P_Y , and P_Z are passed directly to the next step as a no-twirl case.

Step 4: Construct a circuit table based on the protocol circuit:

We developed a quantum circuit simulator in MATLAB. In this model, based on the input defined in Step 1, possible errors are added at the beginning of the main circuit. Then, using the stabilizer formalism, the circuit is evaluated gate by gate to calculate the resulting states. Consequently, each outcome of the circuit corresponds to a specific combination of input errors. Finally, this process generates a table that lists all possible cases, showing the output (I, X, Y, Z, or discard) along with the corresponding input errors.

Step 5: Calculate the results:

Based on the probabilities obtained in Step 3 and the circuit table generated in Step 4, we can summarize the overall probabilities of P_I , P_X , P_Y , P_Z , and discard corresponding to each input fidelity. Since discard events occur in this step, the probabilities of P_I , P_X , P_Y , and P_Z must be renormalized using the formula below.

$$P_{\text{discard}} = 1 - P_I - P_X - P_Y - P_Z \quad (23)$$

$$F_{\text{out}} = P_{I_{\text{out}}} = \frac{P_I}{1 - P_{\text{discard}}} \quad (24)$$

$$P_{A_{\text{out}}} = \frac{P_A}{1 - P_{\text{discard}}}, A = X, Y, Z \quad (25)$$

Step 6: Calculate the rate and discard probability:

The total discard probability up to the current round is given by

$$P_{\text{total discard}} = P_{\text{last discard}} + (1 - P_{\text{last discard}})P_{\text{discard}}, \quad (26)$$

where $P_{\text{last discard}}$ is the total discard probability accumulated up to the previous round, and P_{discard} is the discard probability for the current round. Therefore, the total rate for the current round is

$$R_{\text{total}} = \frac{1}{2^n}(1 - P_{\text{total discard}}), \quad (27)$$

where n is the number of the current round.

Step 7: Loop or output:

Return to Step 3, using the output of the current round as the input for the next round. Alternatively, stop at the current round to generate and plot the results.

C. BBPSSW and DEJMPS

There are many types of 1G protocols, but the first well-known ones are BBPSSW [11] and DEJMPS [12].

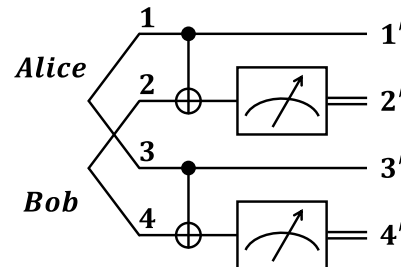


Fig. 11: BBPSSW circuit diagram

The BBPSSW protocol operates as follows: after generating two Bell pairs (1 and 3, 2 and 4), Alice and Bob apply a CNOT gate, using one pair as the control and the other as the target, and then perform measurements on the target pair. If 2' and 4' match, the Bell pair 1' and 3' is kept. Otherwise, the Bell pair is discarded. After each round, BBPSSW requires a twirling operation to ensure that the protocol converges efficiently.

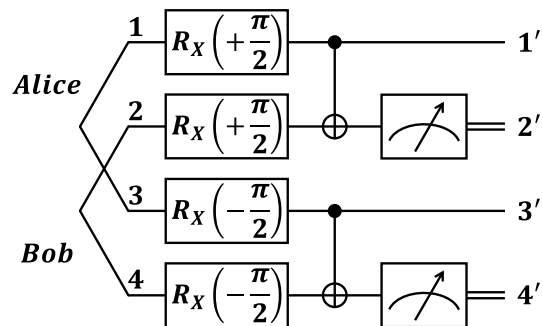


Fig. 12: DEJMPS circuit diagram

The DEJMPS protocol is a modified version of BBPSSW that adds an X-axis rotation to the circuit. Interestingly, if DEJMPS also performs twirling, its performance becomes nearly identical to that of BBPSSW. However, DEJMPS typically omits the twirling step because the asymmetry of Z errors relative to X and Y introduces a bias that allows DEJMPS to converge much faster than BBPSSW.

In the DEJMPS circuit, the $R_X(\pi/2)$ gate transforms the stabilizer group $\{X, Y, Z\}$ into $\{X, Z, -Y\}$, while $R_X(-\pi/2)$ gate transforms $\{X, Y, Z\}$ into $\{X, -Z, Y\}$, according to the rotation operator $R_X(\theta) = e^{-i\frac{\theta X}{2}}$.

In Fig. 13, we compared the output fidelity as a function of the input fidelity over multiple rounds in a single-link scenario for BBPSSW (twirled/no twirl) and DEJMPS (twirled/no twirl) respectively. We can clearly see that all protocols exhibit the same output fidelity in the first round. However, starting from the second round, DEJMPS achieves a higher fidelity than BBPSSW for the same number of rounds. In particular, when focusing on input fidelities greater than 0.5 and beginning from the second round, the following relation can be observed:

$$\begin{aligned} \text{DEJMPS(no twirl)} &> \text{DEJMPS(twirled)} \\ &= \text{BBPSSW(twirled)} \\ &> \text{no coding} \\ &> \text{BBPSSW(no twirl)}. \end{aligned} \quad (28)$$

Therefore, unless stated otherwise, for the rest of this paper “DEJMPS” refers to the protocol without twirling between rounds, whereas “BBPSSW” refers to the protocol with twirling applied after each round.

In the literature, the BBPSSW protocol [11] is often summarized by the closed-form recurrence for the Werner-state fidelity derived in the original paper. Since the protocol first symmetrizes an arbitrary two-qubit mixed state into a Werner state that is fully characterized by the single parameter F , this fidelity-only description does not track the evolution of individual Pauli-error components and therefore cannot explain how a bias in the Pauli error distribution arises during the process.

$$F_{\text{out}} = \frac{F_{\text{in}}^2 + \frac{1}{9}(1 - F_{\text{in}})^2}{F_{\text{in}}^2 + \frac{2}{3}F_{\text{in}}(1 - F_{\text{in}}) + \frac{5}{9}(1 - F_{\text{in}})^2}. \quad (29)$$

The F_{out} from the previous round serves as the input for the next round. This approach works well when we consider only the twirling case. However, when we want to compare it with the no twirling case in DEJMPS, the formula is not sufficient to capture the underlying details. In the original DEJMPS paper [12], the authors introduce a quantum privacy amplification procedure that tracks the Bell-basis populations. The map is formulated in terms of the Bell-diagonal parameters A , B , C , and D , but it does not directly expose the associated $I/X/Y/Z$ Pauli-error components, which makes the error-level interpretation less transparent. To make this connection explicit, we provide the following formula, which is derived based on the contribution of each error combination used to generate the final result.

For BBPSSW,

$$P_I = P_{I_{\text{in}}}^2 + P_{Z_{\text{in}}}^2, \quad (30)$$

$$P_X = P_{X_{\text{in}}}^2 + P_{Y_{\text{in}}}^2, \quad (31)$$

$$P_Y = 2P_{X_{\text{in}}}P_{Y_{\text{in}}}, \quad (32)$$

$$P_Z = 2P_{I_{\text{in}}}P_{Z_{\text{in}}}. \quad (33)$$

For DEJMPS,

$$P_I = P_{I_{\text{in}}}^2 + P_{Y_{\text{in}}}^2, \quad (34)$$

$$P_X = P_{X_{\text{in}}}^2 + P_{Z_{\text{in}}}^2, \quad (35)$$

$$P_Y = 2P_{X_{\text{in}}}P_{Z_{\text{in}}}, \quad (36)$$

$$P_Z = 2P_{I_{\text{in}}}P_{Y_{\text{in}}}. \quad (37)$$

Of course, the probabilities must be renormalized before being used as the input for the next round:

$$P_{\text{discard}} = 1 - P_I - P_X - P_Y - P_Z, \quad (38)$$

$$F_{\text{out}} = P_{I_{\text{out}}} = \frac{P_I}{1 - P_{\text{discard}}}, \quad (39)$$

$$P_{A_{\text{out}}} = \frac{P_A}{1 - P_{\text{discard}}}, \quad A = X, Y, Z. \quad (40)$$

Using the BBPSSW protocol as an example, we can show that when the input fidelity satisfies $P_{I_{\text{in}}} = P_{X_{\text{in}}} + P_{Y_{\text{in}}} + P_{Z_{\text{in}}} = 0.5$, the output fidelity always remains $P_{I_{\text{out}}} = 0.5$:

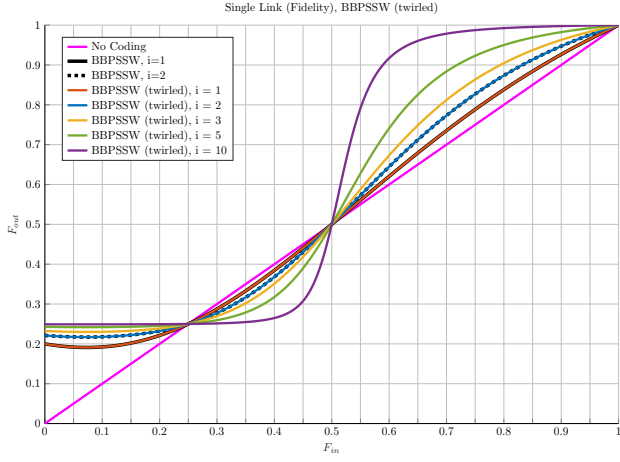
$$\begin{aligned} P_I &= P_{I_{\text{in}}}^2 + P_{Z_{\text{in}}}^2 \\ &= (P_{X_{\text{in}}} + P_{Y_{\text{in}}} + P_{Z_{\text{in}}})^2 + P_{Z_{\text{in}}}^2 \\ &= P_{X_{\text{in}}}^2 + P_{Y_{\text{in}}}^2 + 2P_{Z_{\text{in}}}^2 \\ &\quad + 2P_{X_{\text{in}}}P_{Y_{\text{in}}} + 2P_{Y_{\text{in}}}P_{Z_{\text{in}}} + 2P_{X_{\text{in}}}P_{Z_{\text{in}}} \\ &= (P_{X_{\text{in}}}^2 + P_{Y_{\text{in}}}^2) + 2P_{X_{\text{in}}}P_{Y_{\text{in}}} \\ &\quad + 2(P_{X_{\text{in}}} + P_{Y_{\text{in}}} + P_{Z_{\text{in}}})P_{Z_{\text{in}}} \\ &= P_X + P_Y + P_Z. \end{aligned} \quad (41)$$

Based on the formulas from BBPSSW and DEJMPS, we can observe that the $R_X(\pi/2)$ and $R_X(-\pi/2)$ rotations simply switch P_Z and P_Y . However, this modification makes DEJMPS a highly effective bias strategy.

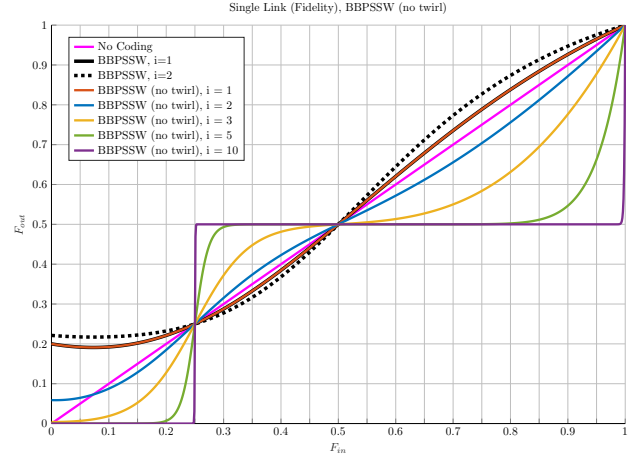
Furthermore, to understand how the bias provides an advantage in DEJMPS (no twirl), we first need to examine how BBPSSW behaves in the no-twirling case.

In Fig. 14, we show the evolution of the I, X, Y, and Z error components over successive rounds for BBPSSW (no twirl) and DEJMPS (no twirl). We can observe that regardless of whether the protocol is BBPSSW (no twirl) or DEJMPS (no twirl), the probability of a Z error is always higher than that of the other errors. Therefore, we refer to these as “bias-on-Z protocols.” In such protocols, we find that the X and Y errors exhibit the primary decreasing trend.

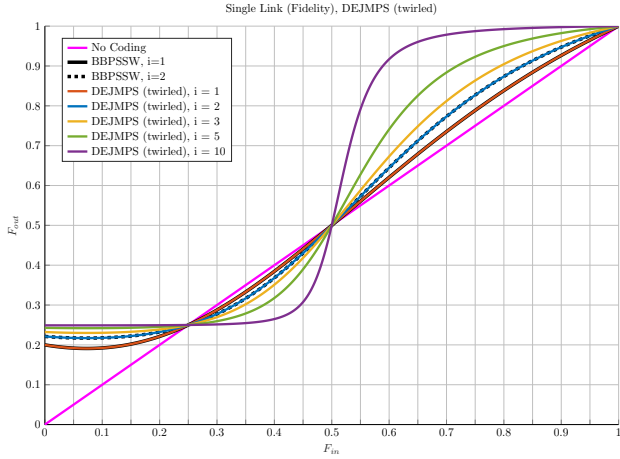
As a result, after DEJMPS (no twirl) applies $R_X(\pi/2)$ and $R_X(-\pi/2)$, the roles of P_Y and P_Z are effectively swapped. Using this insight, we perform a detailed analysis of BBPSSW and DEJMPS without twirling in Appendix I. The calculations show that, because P_Y and P_Z swap, the recursive equations for P_I and P_Z imply that P_I goes to 1 and P_Z goes to 0 for DEJMPS, whereas both go to 0.5 for BBPSSW. This agrees with the plot in Fig. 14.



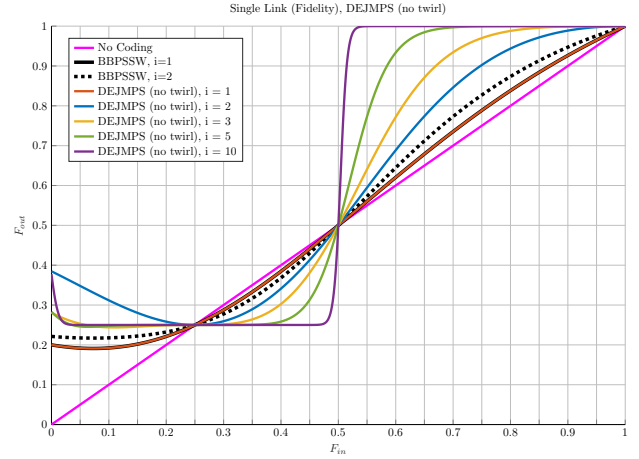
(a) BBPSSW (twirled)



(b) BBPSSW (no twirl)



(c) DEJMPS (twirled)



(d) DEJMPS (no twirl)

Fig. 13: Comparison of the fidelities obtained using BBPSSW and DEJMPS, including both the twirled and no-twirl versions. All cases start from an input fidelity based on the depolarizing channel, and the decision to apply twirling or no-twirling in each round follows the definition of each protocol. “No Coding” indicates that $F_{\text{in}} = F_{\text{out}}$, and i denotes the number of rounds. The black solid and black dashed lines are calculated based on Eq. 29, while the other results are obtained from our circuit simulator.

Theorem 1. Consider the BBPSSW protocol. Let $P_{I_{\text{in}}} = a_0$, $P_{X_{\text{in}}} = b_0$, $P_{Y_{\text{in}}} = c_0$, $P_{Z_{\text{in}}} = d_0$, where the subscript denotes the number of rounds. Assume

$$\begin{aligned}
 a_0 &> \frac{1}{2}, \\
 b_0 &> 0, c_0 > 0, d_0 > 0, \\
 a_0 + b_0 + c_0 + d_0 &= 1, \\
 P_{I_n} &= a_n^2 + d_n^2, \\
 P_{X_n} &= b_n^2 + c_n^2, \\
 P_{Y_n} &= 2b_n c_n, \\
 P_{Z_n} &= 2a_n d_n, \\
 P_{T_n} &= P_{I_n} + P_{X_n} + P_{Y_n} + P_{Z_n}, \\
 a_{n+1} &= \frac{P_{I_n}}{P_{T_n}},
 \end{aligned}$$

$$\begin{aligned}
 b_{n+1} &= \frac{P_{X_n}}{P_{T_n}}, \\
 c_{n+1} &= \frac{P_{Y_n}}{P_{T_n}}, \\
 d_{n+1} &= \frac{P_{Z_n}}{P_{T_n}}.
 \end{aligned}$$

Then, as $n \rightarrow \infty$, we have

$$\begin{aligned}
 a_n + d_n &\rightarrow 1, \\
 b_n + c_n &\rightarrow 0, \\
 a_n &\rightarrow 0.5, \\
 d_n &\rightarrow 0.5, \\
 b_n &\rightarrow 0, \\
 c_n &\rightarrow 0.
 \end{aligned}$$

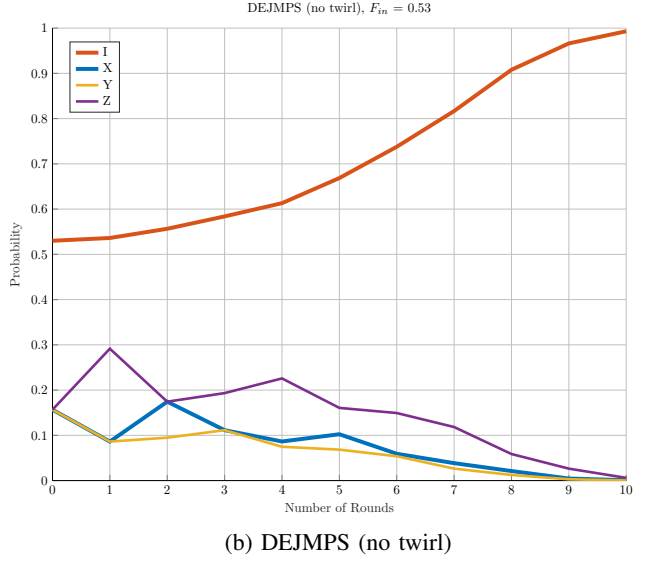
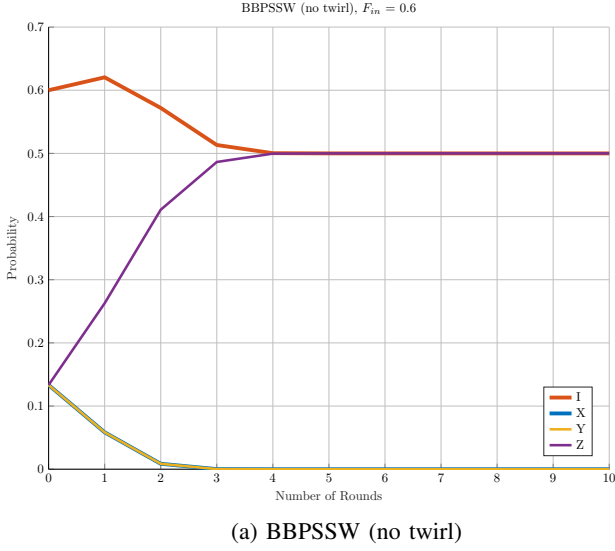


Fig. 14: As a function of the number of rounds, we show how the probabilities of I , X , Y , and Z evolve. To a large extent, DEJMPS (no twirl) can be viewed as BBPSSW (no twirl) with an added R_X rotation gate. Therefore, it is necessary to compare how the bias behaves in both protocols. To illustrate this clearly, we set $F_{\text{in}} = 0.6$ for BBPSSW without twirling and $F_{\text{in}} = 0.53$ for DEJMPS without twirling, so that we can show in detail how the bias evolves round by round.

Proof: See Appendix I-A. ■

Theorem 2. Consider the DEJMPS protocol. Let $P_{I_{\text{in}}} = a_0$, $P_{X_{\text{in}}} = b_0$, $P_{Y_{\text{in}}} = c_0$, $P_{Z_{\text{in}}} = d_0$, where the subscript denotes the number of rounds. Assume

$$\begin{aligned}
 a_0 &> \frac{1}{2}, \\
 b_0 &> 0, c_0 > 0, d_0 > 0, \\
 a_0 + b_0 + c_0 + d_0 &= 1, \\
 P_{I_n} &= a_n^2 + c_n^2, \\
 P_{X_n} &= b_n^2 + d_n^2, \\
 P_{Y_n} &= 2b_n d_n, \\
 P_{Z_n} &= 2a_n c_n, \\
 P_{T_n} &= P_{I_n} + P_{X_n} + P_{Y_n} + P_{Z_n}, \\
 a_{n+1} &= \frac{P_{I_n}}{P_{T_n}}, \\
 b_{n+1} &= \frac{P_{X_n}}{P_{T_n}}, \\
 c_{n+1} &= \frac{P_{Y_n}}{P_{T_n}}, \\
 d_{n+1} &= \frac{P_{Z_n}}{P_{T_n}}.
 \end{aligned}$$

Then, as $n \rightarrow \infty$, we have

$$\begin{aligned}
 a_n + d_n &\rightarrow 1, \\
 b_n + c_n &\rightarrow 0, \\
 a_{n+1} &\rightarrow \frac{a_n^2 + c_n^2}{(a_n + c_n)^2} = 1, \\
 d_{n+1} &\rightarrow \frac{2a_n c_n}{(a_n + c_n)^2} = 0,
 \end{aligned}$$

$$\begin{aligned}
 b_n &\rightarrow 0, \\
 c_n &\rightarrow 0.
 \end{aligned}$$

Proof: See Appendix I-B. ■

The goal of using a 1G protocol is to solve the problem that when the input fidelity is lower than the pseudo-threshold of 2G protocols, the 2G protocol will reduce the output fidelity instead of improving it. Therefore, for low input fidelity, we need to select a 1G protocol that uses fewer discarded Bell pairs while still providing a fidelity improvement. Since we use a depolarizing channel in the first round, the bias begins to provide a benefit starting from the second round.

For the discard probability in BBPSSW, we can easily calculate the value for the first round based on the denominator of Eq. 29:

$$P_{\text{discard}} = 1 - (F_{\text{in}}^2 + \frac{2}{3}F_{\text{in}}(1 - F_{\text{in}}) + \frac{5}{9}(1 - F_{\text{in}})^2). \quad (42)$$

However, starting from the second round, we need to use Eq. 26 to obtain the total discard probability.

In Fig. 15, we compare the total discard probability as a function of the input fidelity over different numbers of rounds for BBPSSW (twirled) and DEJMPS (no twirl), respectively.

Comparing Fig. 15 with Fig. 13a and Fig. 13d, we can obtain some numerical results. Since we focus on the low input-fidelity region, it is appropriate to consider the case where $F_{\text{in}} = 0.6$ for the discussion.

When $i = 2$, we find that DEJMPS discards 5.69% more Bell pairs than BBPSSW, but the fidelity is improved by 6.82%. As the number of rounds increases, this benefit becomes more and more significant. When $i = 3$, we find that DEJMPS discards 3.89% more Bell pairs than BBPSSW, but the fidelity is improved by 14.72%.

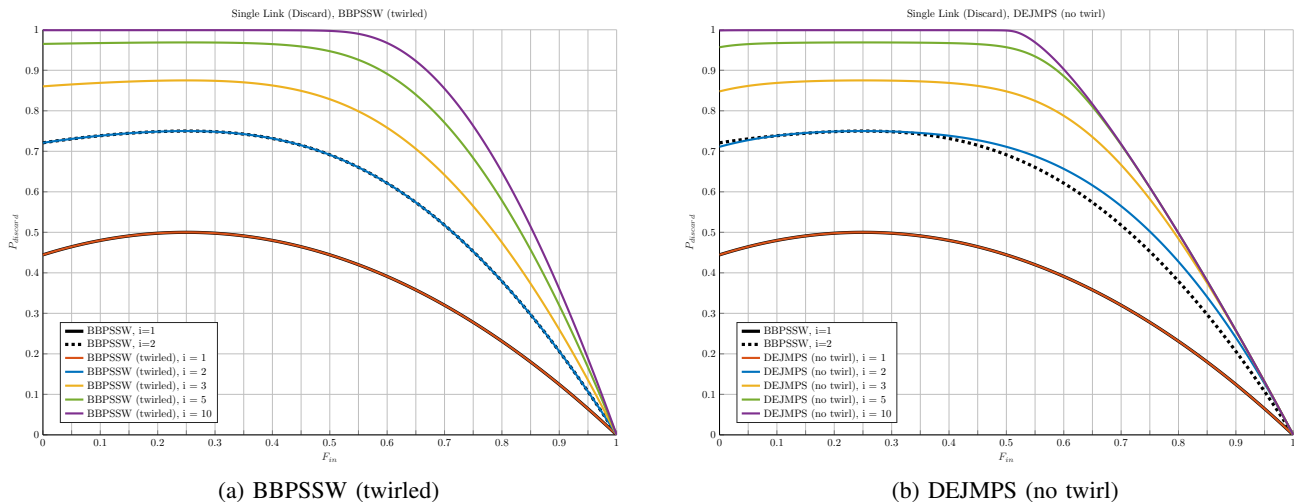


Fig. 15: Comparison of discard probabilities and fidelities between DEJMPS in 13d and BBPSSW in 13a for different round numbers. As an example, for $F_{\text{in}} = 0.6$, when $i = 2$ (rounds), DEJMPS discards 0.65661 of the Bell pairs while BBPSSW discards 0.621285, which is 0.035325 (5.69%) more. The output fidelity of DEJMPS is 0.688616, compared to 0.644639 for BBPSSW, an improvement of 0.043977 (6.82%). When $i = 3$, DEJMPS discards 0.78774 of the Bell pairs while BBPSSW discards 0.758215, which is 0.029525 (3.89%) more. The output fidelity of DEJMPS is 0.77193, compared to 0.67288 for BBPSSW, an improvement of 0.09905 (14.72%).

Therefore, we can see that as the number of rounds increases, DEJMPS continues to improve rapidly in the low input-fidelity region. In almost all performance comparisons, DEJMPS outperforms other 1G protocols. For this reason, we select DEJMPS as the representative 1G protocol for our analysis and use it as the benchmark for comparison with 2G protocols.

D. Comparison of 1G and 2G Protocols without Repeaters

For the 2G protocols, we considered the quantum error-correcting codes $[[9, 1, 3]]$, $[[9, 2, 3]]$, and $[[9, 3, 3]]$. These codes exhibit relatively high input fidelity thresholds (or pseudo-thresholds). Therefore, before reaching these thresholds, it is necessary to apply 1G protocols to boost the input fidelity to a level where 2G distillation becomes effective.

Taking $[[9, 3, 3]]$ as an example (previously introduced in Section I), we select this code because its effective rate is approximately $1/3$, compared with $1/9$ for the $[[9, 1, 3]]$ code, while maintaining the same communication distance. The threshold input fidelity for the $[[9, 3, 3]]$ code is around 0.9563, meaning that 1G purification must first raise the fidelity from the low input-fidelity region (e.g., between 0.5 and 0.8) to this threshold before any 2G correction can be meaningfully applied.

In Fig. 16, we compare the output fidelity as a function of the input fidelity for the 1G, 2G, and hybrid cases. In particular, you can clearly see that the curve is not continuous when 1G is included in the protocol. Whenever the curve has a discontinuous jump, we call the turning point a “checkpoint”. This checkpoint is important because it marks where the protocol jumps to a different number of rounds. When $F_{\text{in}} = 0.5$, no matter how many rounds we execute, the output fidelity

always remains 0.5. Therefore, in Fig. 16, the x-axis range for the input fidelity is set from 0.501 to 1.

After the fidelity is boosted above the code threshold by 1G purification, a single round of 2G QEC is performed on that purified state. The output fidelity obtained after this QEC step serves as the target benchmark. We then examine the minimum number of DEJMPS rounds required to achieve an output fidelity that is not lower than the benchmark purely through purification. When the input fidelity is higher, each round still improves the fidelity, but the improvement in each new round is smaller than in the previous round. Thus, a single round is sufficient to achieve the target fidelity over a wider range when the input fidelity is already high. As a result, only a few checkpoints appear in the high-fidelity region, while more checkpoints are observed when the input fidelity is close to 0.5.

In Fig. 17, we show, as a function of the input fidelity, the number of rounds needed to reach the target output fidelity for protocols that involve 1G. Interestingly, the results show that only one or two additional DEJMPS rounds are sufficient to reach the target benchmark after several DEJMPS rounds have raised the fidelity to the pseudo-threshold. Because only a single round of 2G QEC is performed, the total number of rounds required for purely 1G purification and the hybrid 1G+2G approach becomes the same in most cases.

Once we determine the required number of DEJMPS rounds, we can calculate the corresponding rate, where the discard probability is included as part of the efficiency, such that $R_{\text{out}} = \frac{n_{\text{out}}}{n_{\text{in}}} (1 - P_{\text{total discard}})$, where n_{in} and n_{out} represent the total number of input and output Bell pairs, respectively. Therefore, these quantities must be evaluated separately for the 1G, 2G, and hybrid 1G+2G cases.

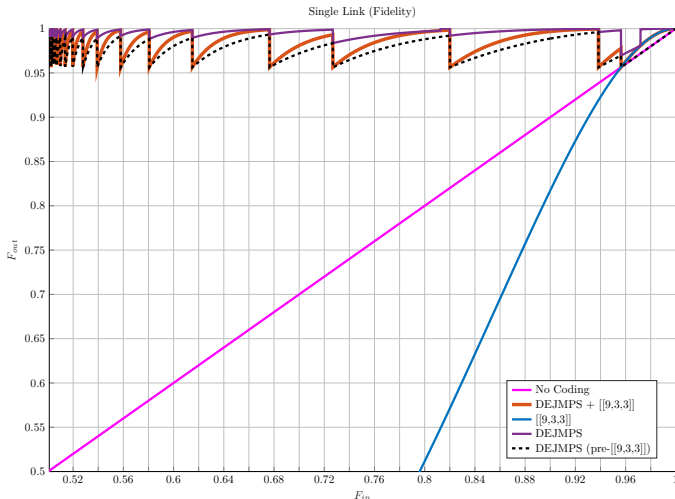


Fig. 16: The $F_{\text{in}}-F_{\text{out}}$ mapping for the case without repeaters. DEJMPS (pre- $[[9, 3, 3]]$) refers to applying several rounds of DEJMPS until the fidelity reaches or exceeds the pseudo-threshold of $[[9, 3, 3]]$. Then, one additional round of $[[9, 3, 3]]$ coding is performed to obtain DEJMPS+ $[[9, 3, 3]]$. Finally, we set the fidelity achieved by DEJMPS+ $[[9, 3, 3]]$ as the target and determine the minimum number of DEJMPS rounds required to match or surpass it. As the input fidelity increases, low-round DEJMPS yields only a modest improvement in the output fidelity. As a result, the range of input fidelities for which the same (low) number of rounds remains optimal becomes broader. Consequently, these low-round settings apply over a larger portion of the input-fidelity regime and contribute more to the overall fidelity improvement of the protocol. Therefore, when using DEJMPS to raise the fidelity toward the pseudo-threshold, the plot displays several “checkpoints” (jumps) indicating when to reduce the minimum required number of rounds to reach the pseudo-threshold.

1) *Purely 1G*: When discussing the purely 1G case, the rate calculation is straightforward. In DEJMPS, each round consumes two input Bell pairs to produce one output Bell pair or a discard. This means that once the number of DEJMPS rounds i is known, the rate can be directly obtained as follows:

$$R_{\text{out}} = \frac{1}{2^i} (1 - P_{\text{total discard}}). \quad (43)$$

2) *Purely 2G*: Since this section considers only a single 2G round and there is no discard in the purely 2G case, the rate can be directly determined by the code used. If we use a $[[n, k, d]]$ code, the rate can be obtained as follows:

$$R_{\text{out}} = \frac{k}{n}. \quad (44)$$

3) *Hybrid 1G+2G*: In our case, when using the hybrid strategy, several rounds of DEJMPS are performed first, followed by a single round of 2G QEC. Therefore, the rate can be obtained by combining Eq. 43 and Eq. 44, when a $[[n, k, d]]$ code is used for the 2G stage, as follows:

$$R_{\text{out}} = \frac{k}{2^i n} (1 - P_{\text{total discard}}). \quad (45)$$

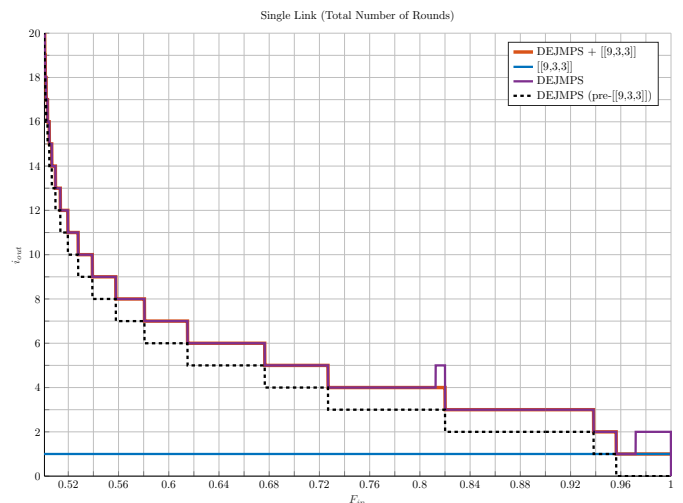


Fig. 17: The $F_{\text{in}}-i_{\text{out}}$ mapping for the case without repeaters. This plot shows the relationship between the input fidelity and the number of required protocol rounds. Several rounds of DEJMPS are applied to increase the input fidelity until it reaches the pseudo-threshold of $[[9, 3, 3]]$. Once the input fidelity is at or above this pseudo-threshold, DEJMPS rounds are no longer used and a single round of 2G QEC is applied instead, minimizing the total number of rounds required and avoiding unnecessary Bell-pair discards. We can observe that the difference between DEJMPS (pre- $[[9, 3, 3]]$) and DEJMPS+ $[[9, 3, 3]]$ is typically only one additional round, and only a few cases require two rounds. This means that in most cases, the number of rounds required for DEJMPS and DEJMPS+ $[[9, 3, 3]]$ is the same.

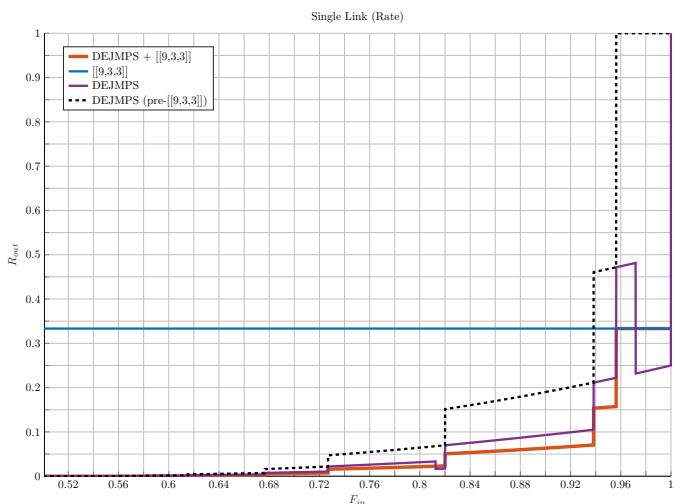


Fig. 18: The $F_{\text{in}}-R_{\text{out}}$ mapping for the case without repeaters. In this plot, we consider the discard probability $P_{\text{total discard}}$ as part of the 1G rate, such that $R_{\text{out}} = \frac{n_{\text{out}}}{n_{\text{in}}} (1 - P_{\text{total discard}})$.

In Fig. 18, we compare the rates for the 1G, 2G, and hybrid cases. We observe that the discard probability $P_{discard}$ does not significantly affect the rate when DEJMPS is involved. Moreover, since the rate of the $[[9, 3, 3]]$ code is always $\frac{1}{3}$, while the rate for strategies involving DEJMPS depends heavily on the number of rounds, the $[[9, 3, 3]]$ code maintains an advantage in most cases.

However, when examining the fidelity results in Fig. 16, and the zoomed-in version in Fig. 19b that will be discussed in the next section, we observe that the $[[9, 3, 3]]$ code does not provide any fidelity advantage. This indicates that we need to develop another metric to evaluate the efficiency of strategies involving 1G purification.

E. Exploring an Efficiency Function for Hybrid 1G+2G Protocols Without Repeaters

A new efficiency metric is required, because it not only allows us to determine which strategy involving 1G purification performs better, but also indicates when to switch from one protocol to another. In the previous section, we introduced an efficiency function to describe the 2G QEC strategy under different repeater scenarios and used it to determine the optimal switching point between protocols:

$$E(F_{in}) = \frac{n_{out}D(F_{out}(F_{in}))}{n_{in}D(F_{in})}. \quad (46)$$

However, when 1G purification is involved, the discard probability $P_{discard}$ must be included in the formula. Although it is not the primary factor affecting the overall trend of the curve, it reflects the intrinsic behavior of the 1G protocol. Therefore, we update the efficiency function as follows:

$$E(F_{in}) = \frac{n_{out}D(F_{out}(F_{in}))}{n_{in}D(F_{in})}(1 - P_{total\ discard}). \quad (47)$$

In Fig. 19, we show the efficiency and the corresponding output fidelity as functions of the input fidelity. We compute the efficiency using the function introduced in the previous section for 2G protocols. We can see that this metric still effectively characterizes 1G purification. The efficiency curve behaves consistently as expected when $F_{in} > 0.81071$. However, when $F_{in} < 0.81071$, we have $D(F_{in}) < 0$, which results in $E(F_{in}) < 0$. In particular, at $F_{in} = 0.81071$, $D(F_{in}) = 0$, causing $E(F_{in})$ to diverge to infinity.

In fact, when examining Fig. 16, there are several pieces of information that we aim to extract from the efficiency function, which become difficult to obtain when 1G purification is involved.

- 1) We aim to identify the precise checkpoints of the output fidelity from the efficiency function. However, this becomes difficult when the input fidelity is close to or below 0.81071, because $D(F_{in}) \leq 0$ in that region.
- 2) We aim to determine which strategy provides a better benefit for the same input fidelity. A better strategy should exhibit higher efficiency than the others. However, once $D(F_{in}) < 0$, the preferred strategy may instead show a lower efficiency than the alternatives.
- 3) Although this is not essential, to ensure that the efficiency behaves like a proper efficiency metric, we may apply

normalization or a similar scaling process to keep the results within the range $[0, 1]$.

The first issue we need to address is that $D(F_{in}) \leq 0$. Since $D(F_{in})$ appears in the denominator of our efficiency function, this prevents us from using F_{in} directly as the reference variable. Moreover, because 1G protocols generate multiple checkpoints, an appropriate way to redefine the efficiency function is to incorporate DEJMPS performance into the metric.

After several attempts, we found that using the minimum number of DEJMPS rounds required to reach a distillable entanglement of 0.12 is a reasonable strategy to include in our efficiency function. Thus, we update the efficiency function as follows:

$$E(F_{in}) = \frac{n_{out}D(F_{out}(F_{in}))}{n_{in}D(F_{in})_{DEJMPS \geq 0.12}}(1 - P_{total\ discard}). \quad (48)$$

Since we want the efficiency to reflect a balance between the communication rate and the distillable entanglement, we do not modify the other components of the metric. Meanwhile, we expect the efficiency to remain below one. Through extensive checks, we found that 0.12 serves as an effective threshold for the input distillable entanglement. Here, $D(F_{in})_{DEJMPS \geq 0.12}$ indicates that if the input distillable entanglement is below 0.12, a minimum number of DEJMPS rounds must be applied to raise it to at least 0.12. If the input distillable entanglement is already greater than 0.12, no purification is needed at this stage. Finally, these two cases are combined into the unified formulation of the input distillable entanglement in the efficiency function. Since our goal here is only to address the issues arising from $D(F_{in})$, we continue to use the total numbers for n_{in} and n_{out} without excluding the DEJMPS rounds in the baseline.

To address the issue that the efficiency may become negative when the output fidelity is lower than 0.81071, we simply set any negative efficiency value to zero. Therefore, the final efficiency function is given below:

$$E(F_{in}) = \max \left\{ \frac{n_{out}D(F_{out}(F_{in}))}{n_{in}D(F_{in})_{DEJMPS \geq 0.12}}(1 - P_{total\ discard}), 0 \right\}. \quad (49)$$

In Fig. 20, we plot the efficiency computed using the updated efficiency function, along with the corresponding distillable entanglement. We can see that the new efficiency function can clearly reveal the checkpoints corresponding to the output fidelity. The better strategy consistently exhibits a higher efficiency, and the resulting values remain within the range between 0 and 1.

The only remaining issue is that when the DEJMPS baseline reaches a checkpoint but the protocol under evaluation does not, the efficiency function still displays a checkpoint artifact. For example, when the input fidelity is around 0.84, there should clearly be no checkpoint for any protocol. However, the efficiency function still displays one, simply because the DEJMPS baseline reaches a checkpoint at that point.

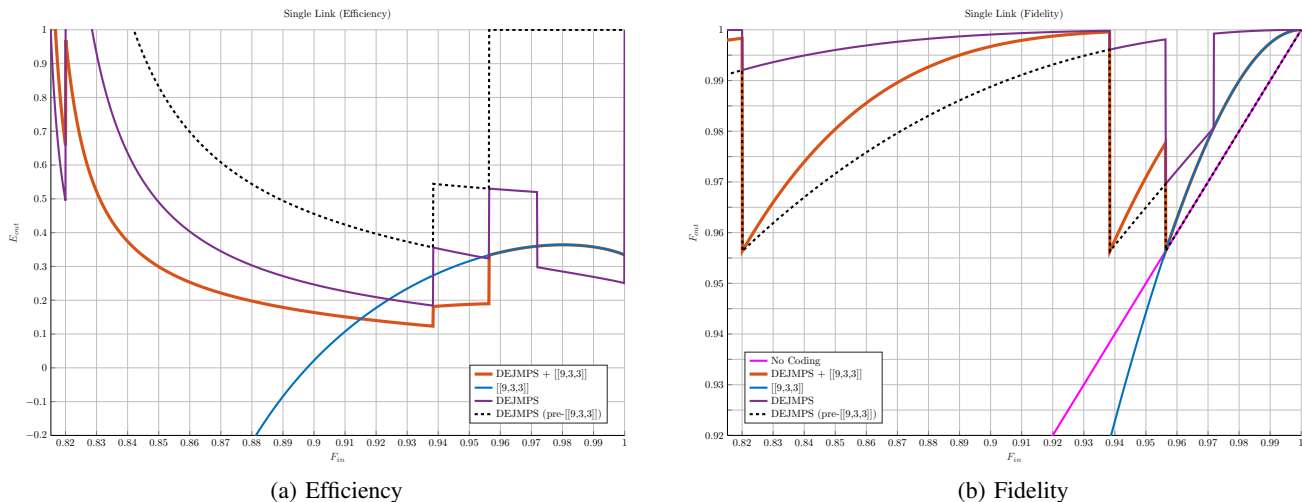


Fig. 19: Using the previously defined formula to generate the efficiency function, we observe that as the input fidelity approaches 0.81071, the efficiency function becomes increasingly unstable until it diverges to infinity. In contrast, when the input fidelity is greater than 0.81071, the efficiency function accurately captures all critical points corresponding to the output fidelity.

Since we aim to develop a general version of the efficiency function that can be applied to any type of protocol without modifying the baseline, the strategy we propose provides a good balance among all relevant factors.

VI. CONCLUSION

In this work, we considered a linear chain of repeaters that create entanglement with neighboring repeaters, perform quantum error correction-based entanglement distillation, execute entanglement swaps, and repeat the process until the end nodes have sufficient number of high-fidelity Bell pairs. We introduced a novel adaptive strategy to switch between different codes for each round of distillation, as a function of the network operating point. Using three 9-qubit codes with increasing rates, we conducted simulations to compare four different protocols that perform three rounds of distillation, independent of the number of repeaters. As our end-to-end metric, we defined a function called the *efficiency*, which depends on the protocol rate as well as input and output distillable entanglement, which in turn depends on the input and output fidelities. We conclusively demonstrated the advantages of the adaptive strategy to maximize the efficiency, where each of the four protocols become optimal for a certain region of input fidelity.

Subsequently, we combined our protocols with non-error correction-based entanglement purification protocols that have significantly smaller input fidelity thresholds. We first showed that DEJMPS comprehensively outperforms BBPSSW aided by its asymmetric output error profile. Then, for input fidelities below the code threshold, we began with DEJMPS rounds to cross the threshold and compared two strategies: adaptively switching to one round of code-based distillation or continuing with DEJMPS to achieve the same performance. We highlighted the emergence of “checkpoints” in the fidelity plot due to the periodic decrease of required number of DEJMPS rounds with increase in input fidelity. We observed

that the rapid improvement of fidelity with each DEJMPS round makes it superior to the code when considering only the output fidelity. But with a refined efficiency metric that combines rate and fidelity, the code emerges at the top when the input fidelity is very high. This illuminates the importance of choosing the code and purification protocol as a function of the network operating point, thereby extending the results from the earlier adaptive coding strategy. We expect that such a streamlined strategy will have several practical advantages in real networks.

In future work, we will extend this work to realistic noise scenarios and consider fault-tolerant schemes for performing distillation and swaps. Specifically, we will examine the best approaches to pick adaptive code and protocol sequences, the fault-tolerance requirements, the associated resource estimates, and practical considerations. Such studies will clearly establish the evolution from first to second generation repeaters and beyond. In the past [13], we considered optimal schedules for distillation and swaps at each repeater to maximize end-to-end distillable entanglement and also calculated memory requirements in the repeaters. These schedules and resource requirements can be adapted to the adaptive distillation setting introduced in this work. We have also considered schemes for Bell pair distillation in trapped-ion repeaters [19], so our results can be contextualized for such hardware technologies. We have showed state-of-the-art fidelity thresholds for distilling GHZ states using quantum low-density parity-check (LDPC) codes [15]. This enables a path to extend this adaptive distillation approach to GHZ states, which will play an important role in distributed quantum computing and sensing applications. Overall, our ultimate goal is to find the best adaptive strategies as a function of the desired type of entanglement, the hardware technology, the end-to-end metric, and the network topology.

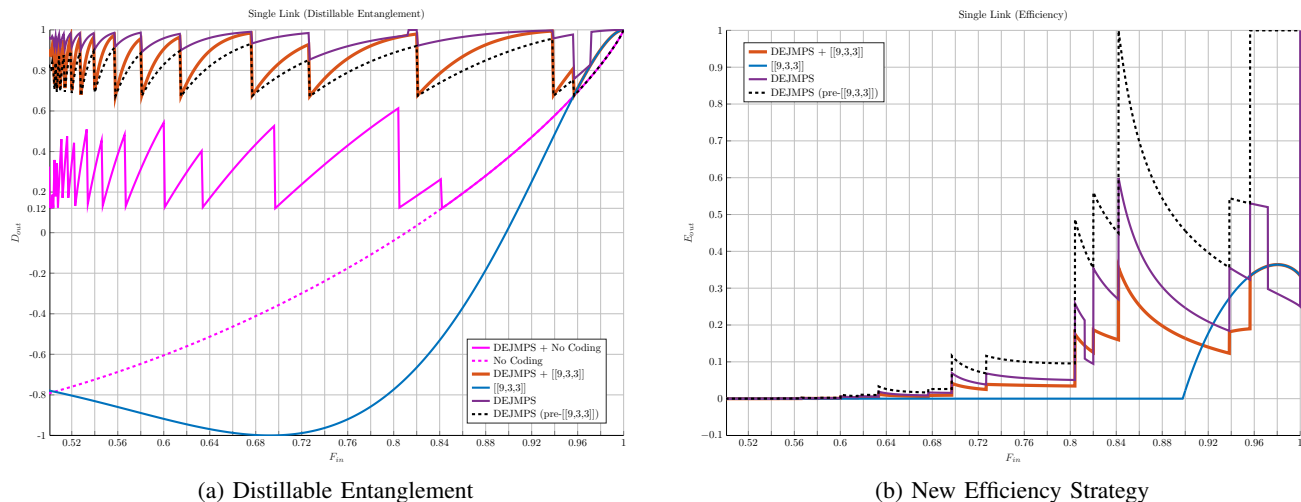


Fig. 20: We adjust the efficiency function by using the DEJMPS + No-Coding strategy as the baseline. This means that we apply the minimum number of DEJMPS rounds required to increase the distillable entanglement to 0.12. If the input fidelity already corresponds to a distillable entanglement above 0.12, the No-Coding curve is used directly. In addition, any part of the efficiency that becomes negative is set to zero.

ACKNOWLEDGMENTS

We would like to thank Kaushik Seshadreesan, Filip Rzepčdek, and Stefan Krastanov for helpful discussions. This work was supported by the U.S. National Science Foundation under the Engineering Research Centers program, Grant no. 1941583 (“Center for Quantum Networks”).

REFERENCES

- [1] S. Pirandola, R. Laurenza, C. Ottaviani, and L. Banchi, “Fundamental limits of repeaterless quantum communications,” *Nature Communications*, vol. 8, pp. 1–15, 4 2017.
- [2] C. H. Bennett, D. P. DiVincenzo, J. A. Smolin, and W. K. Wootters, “Mixed-state entanglement and quantum error correction,” *Physical Review A*, vol. 54, pp. 3824–3851, 11 1996.
- [3] S. Muralidharan, L. Li, J. Kim, N. Lütkenhaus, M. D. Lukin, and L. Jiang, “Optimal architectures for long distance quantum communication,” *Scientific Reports*, vol. 6, p. 20463, 2 2016.
- [4] N. Berthussen, J. Dreiling, C. Foltz, J. P. Gaebler, T. M. Gatterman, D. Gresh, N. Hewitt, M. Mills, S. A. Moses, B. Neyenhuis, P. Siegfried, and D. Hayes, “Experiments with the 4d surface code on a qccd quantum computer,” *arXiv:2408.08865*, 8 2024.
- [5] D. Bluvstein, S. J. Evered, A. A. Geim, S. H. Li, H. Zhou, T. Manovitz, S. Ebadi, M. Cain, M. Kalinowski, D. Hangleiter, J. P. B. Ataides, N. Maskara, I. Cong, X. Gao, P. S. Rodriguez, T. Karolyshyn, G. Semeghini, M. J. Gullans, M. Greiner, V. Vuletić, and M. D. Lukin, “Logical quantum processor based on reconfigurable atom arrays,” *Nature*, vol. 626, pp. 58–65, 2 2024.
- [6] M. P. da Silva, C. Ryan-Anderson, J. M. Bello-Rivas, A. Chernoguzov, J. M. Dreiling, C. Foltz, J. P. Gaebler, T. M. Gatterman, D. Hayes, N. Hewitt, J. Johansen, D. Lucchetti, M. Mills, S. A. Moses, B. Neyenhuis, A. Paz, J. Pino, P. Siegfried, J. Strabley, S. J. Wernli, R. P. Stutz, and K. M. Svore, “Demonstration of logical qubits and repeated error correction with better-than-physical error rates,” *arXiv:2404.02280*, 4 2024.
- [7] R. S. Gupta, N. Sundaresan, T. Alexander, C. J. Wood, S. T. Merkel, M. B. Healy, M. Hillenbrand, T. Joehym-O’Connor, J. R. Wootton, T. J. Yoder, A. W. Cross, M. Takita, and B. J. Brown, “Encoding a magic state with beyond break-even fidelity,” *Nature*, vol. 625, pp. 259–263, 1 2024.
- [8] R. Lescanne, M. Villiers, T. Peronnin, A. Sarlette, M. Delbecq, B. Huard, T. Kontos, M. Mirrahimi, and Z. Leghtas, “Exponential suppression of bit-flips in a qubit encoded in an oscillator,” *Nature Physics*, vol. 16, pp. 509–513, 3 2020.
- [9] B. W. Reichardt, A. Paetznick, D. Aasen, I. Basov, J. M. Bello-Rivas, P. Bonderson, R. Chao, W. van Dam, M. B. Hastings, A. Paz, M. P. da Silva, A. Sundaram, K. M. Svore, A. Vaschillo, Z. Wang, M. Zanner, W. B. Cairncross, C.-A. Chen, D. Crow, H. Kim, J. M. Kindem, J. King, M. McDonald, M. A. Norcia, A. Ryou, M. Stone, L. Wadleigh, K. Barnes, P. Battaglini, T. C. Bohdanowicz, G. Booth, A. Brown, M. O. Brown, K. Cassella, R. Coxe, J. M. Epstein, M. Feldkamp, C. Griger, E. Halperin, A. Heinz, F. Hummel, M. Jaffe, A. M. W. Jones, E. Kapit, K. Kotru, J. Lauigan, M. Li, J. Marjanovic, E. Megidish, M. Meredith, R. Morshead, J. A. Muniz, S. Narayanaswami, C. Nishiguchi, T. Paule, K. A. Pawlak, K. L. Pudenz, D. R. Pérez, J. Simon, A. Smull, D. Stack, M. Urbanek, R. J. M. van de Veedonk, Z. Vendeiro, R. T. Weverka, T. Wilkason, T.-Y. Wu, X. Xie, E. Zaly-Geller, X. Zhang, and B. J. Bloom, “Logical computation demonstrated with a neutral atom quantum processor,” *arXiv:2411.11822*, 11 2024.
- [10] P. S. Rodriguez, J. M. Robinson, P. N. Jepsen, Z. He, C. Duckering, C. Zhao, K.-H. Wu, J. Campo, K. Bagnall, M. Kwon, T. Karolyshyn, P. Weinberg, M. Cain, S. J. Evered, A. A. Geim, M. Kalinowski, S. H. Li, T. Manovitz, J. Amato-Grill, J. I. Basham, L. Bernstein, B. Braverman, A. Bylinskii, A. Choukri, R. Deangelo, F. Fang, C. Fieweger, P. Frederick, D. Haines, M. Hamdan, J. Hammett, N. Hsu, M.-G. Hu, F. Huber, N. Jia, D. Kedar, M. Kornjača, F. Liu, J. Long, J. Lopatin, P. L. S. Lopes, X.-Z. Luo, T. M. Macr’i, O. M. Markovi’c, L. A. Martínez-Martínez, X. Meng, S. Ostermann, E. Ostroumov, D. Paquette, Z. Qiang, Y. Shofman, A. Singh, M. Singh, N. Sinha, H. Thoreen, N. Wan, V. Wang, D. Waxman-Lenz, T. Wong, J. Wurtz, A. Zhdanov, L. Zheng, M. Greiner, A. Keesling, N. Gemelke, V. V. Vuleti’c, T. Kitagawa, S.-T. Wang, D. Bluvstein, M. D. Lukin, A. Lukin, H. Zhou, and S. H. Cantú, “Experimental demonstration of logical magic state distillation,” *arXiv:2412.15165*, 12 2024.
- [11] C. H. Bennett, G. Brassard, S. Popescu, B. Schumacher, J. A. Smolin, and W. K. Wootters, “Purification of noisy entanglement and faithful teleportation via noisy channels,” *Phys. Rev. Lett.*, vol. 76, pp. 722–725, Jan 1996.
- [12] D. Deutsch, A. Ekert, R. Jozsa, C. Macchiavello, S. Popescu, and A. Sanpera, “Quantum privacy amplification and the security of quantum cryptography over noisy channels,” *Phys. Rev. Lett.*, vol. 77, pp. 2818–2821, Sep 1996.
- [13] A. Patil, M. Pacenti, B. Vasić, S. Guha, and N. Rengaswamy, “Entanglement Routing using Quantum Error Correction for Distillation,” *arXiv preprint*, May 2024.
- [14] M. M. Wilde, H. Krovi, and T. A. Brun, “Convolutional entanglement distillation,” in *IEEE International Symposium on Information Theory*, pp. 2657–2661, 8 2010.
- [15] N. Rengaswamy, N. Raveendran, A. Raina, and B. Vasić, “Entanglement purification with quantum LDPC codes and iterative decoding,”

Quantum, vol. 8, p. 1233, 1 2024.

- [16] M. Grassl, "Bounds on the minimum distance of linear codes and quantum codes." Online available at <http://www.codetables.de>, 2007.
- [17] M. A. Nielsen and I. L. Chuang, *Quantum Computation and Quantum Information: 10th Anniversary Edition*. Cambridge University Press, 10th anniversary edition ed., 2010.
- [18] L. Valentini, R. B. Christensen, P. Popovski, and M. Chiani, "Reliable quantum communications based on asymmetry in distillation and coding," *IEEE Transactions on Quantum Engineering*, vol. 5, pp. 1–13, 2024.
- [19] A. Kang, S. Guha, N. Rengaswamy, and K. P. Seshadreesan, "Trapped ion quantum repeaters with entanglement distillation based on quantum LDPC codes," in *IEEE International Conference on Quantum Computing and Engineering (QCE)*, vol. 1, pp. 1165–1171, Institute of Electrical and Electronics Engineers Inc., 2023.
- [20] C. Macchiavello, "On the analytical convergence of the qpa procedure," *Physics Letters A*, vol. 246, no. 5, pp. 385–388, 1998.

APPENDIX I

BBPSSW (NO TWIRL) AND DEJMPS (NO TWIRL)

In [20], Macchiavello's main objective was to establish analytical convergence of the quantum privacy amplification (QPA) map for Bell diagonal states. The paper provides a convergence proof that is not included in the original Deutsch *et al.* protocol [12], where several conclusions are supported by numerical analysis. The treatment is largely framed as an iteration of Bell basis populations, and it is not intended to offer an operational description of how the underlying Pauli error components evolve through the procedure. The monotone used in the proof is introduced as a mathematical device, and its physical meaning is left unclear.

Motivated by these limitations, we develop a more intuitive description at the error level and use it to compare the BBPSSW (no twirl) and DEJMPS (no twirl) protocols. Our study still leverages numerical simulations, but we use them to validate the proposed intuition and to quantify protocol dependent differences under the noise models of interest.

A. BBPSSW (no twirl)

For BBPSSW (no twirl), the main text gives the following relationship:

$$P_I = P_{I_{in}}^2 + P_{Z_{in}}^2, \quad (50)$$

$$P_X = P_{X_{in}}^2 + P_{Y_{in}}^2, \quad (51)$$

$$P_Y = 2P_{X_{in}}P_{Y_{in}}, \quad (52)$$

$$P_Z = 2P_{I_{in}}P_{Z_{in}}, \quad (53)$$

$$P_T = P_I + P_X + P_Y + P_Z, \quad (54)$$

$$P_{I_{out}} = \frac{P_I}{P_T}, \quad (55)$$

$$P_{X_{out}} = \frac{P_X}{P_T}, \quad (56)$$

$$P_{Y_{out}} = \frac{P_Y}{P_T}, \quad (57)$$

$$P_{Z_{out}} = \frac{P_Z}{P_T}. \quad (58)$$

Using this, we want to analytically derive the performance that is observed in Fig. 14.

Proof of Theorem 1: Recall that

$$a_0 > \frac{1}{2},$$

$$b_0 > 0, c_0 > 0, d_0 > 0,$$

$$a_0 + b_0 + c_0 + d_0 = 1,$$

$$P_{I_n} = a_n^2 + d_n^2,$$

$$P_{X_n} = b_n^2 + c_n^2,$$

$$P_{Y_n} = 2b_n c_n,$$

$$P_{Z_n} = 2a_n d_n,$$

$$P_{T_n} = P_{I_n} + P_{X_n} + P_{Y_n} + P_{Z_n},$$

$$a_{n+1} = \frac{P_{I_n}}{P_{T_n}},$$

$$b_{n+1} = \frac{P_{X_n}}{P_{T_n}},$$

$$c_{n+1} = \frac{P_{Y_n}}{P_{T_n}},$$

$$d_{n+1} = \frac{P_{Z_n}}{P_{T_n}}.$$

To prove the result, we first derive the following relationship:

$$P_{I_0} = a_0^2 + d_0^2 \quad (59)$$

$$P_{X_0} = b_0^2 + c_0^2 \quad (60)$$

$$P_{Y_0} = 2b_0 c_0 \quad (61)$$

$$P_{Z_0} = 2a_0 d_0 \quad (62)$$

$$\begin{aligned} P_{T_0} &= P_{I_0} + P_{X_0} + P_{Y_0} + P_{Z_0} \\ &= a_0^2 + d_0^2 + b_0^2 + c_0^2 + 2b_0 c_0 + 2a_0 d_0 \\ &= (a_0 + d_0)^2 + (b_0 + c_0)^2 \end{aligned}$$

$$a_1 = \frac{a_0^2 + d_0^2}{(a_0 + d_0)^2 + (b_0 + c_0)^2} \quad (63)$$

$$b_1 = \frac{b_0^2 + c_0^2}{(a_0 + d_0)^2 + (b_0 + c_0)^2} \quad (64)$$

$$c_1 = \frac{2b_0 c_0}{(a_0 + d_0)^2 + (b_0 + c_0)^2} \quad (65)$$

$$d_1 = \frac{2a_0 d_0}{(a_0 + d_0)^2 + (b_0 + c_0)^2} \quad (66)$$

So,

$$a_1 + d_1 = \frac{(a_0 + d_0)^2}{(a_0 + d_0)^2 + (b_0 + c_0)^2} \quad (67)$$

$$b_1 + c_1 = \frac{(b_0 + c_0)^2}{(a_0 + d_0)^2 + (b_0 + c_0)^2} \quad (68)$$

Let $s = a + d$, $t = b + c$,

$$s_1 = \frac{s_0^2}{s_0^2 + t_0^2} \quad (69)$$

$$t_1 = \frac{t_0^2}{s_0^2 + t_0^2} \quad (70)$$

Let $u = \frac{s}{t}$,

$$u_1 = \frac{s_1}{t_1} = \frac{s_0^2}{t_0^2} = u_0^2 \quad (71)$$

So,

$$u_n = u_{n-1}^2 = u_0^{2^n} \quad (72)$$

Therefore, when $u_0 > 1$ and $n \rightarrow \infty$, we have $u_n \rightarrow \infty$.

Since $u_0 > 1$ implies $s_0 > t_0$, it follows that $F_{I_{in}} + F_{Z_{in}} > F_{X_{in}} + F_{Y_{in}}$. Moreover, as discussed in the main text, $F_{I_{in}} > 0.5$. Therefore, the condition $u_0 > 1$ is always satisfied.

Therefore, as $n \rightarrow \infty$, we have $u_n = \frac{s_n}{t_n} \rightarrow 0$.

So,

$$s_{n+1} = \frac{s_n^2}{s_n^2 + t_n^2} = \frac{\left(\frac{s_n}{t_n}\right)^2}{\left(\frac{s_n}{t_n}\right)^2 + 1} = \frac{(u_n)^2}{(u_n)^2 + 1} \rightarrow 1 \quad (73)$$

$$t_{n+1} = \frac{t_n^2}{s_n^2 + t_n^2} = \frac{1}{\left(\frac{s_n}{t_n}\right)^2 + 1} = \frac{1}{(u_n)^2 + 1} \rightarrow 0 \quad (74)$$

Therefore, as $n \rightarrow \infty$, we have $t_n \rightarrow 0$, and hence $P_{X_{out}}$ and $P_{Y_{out}}$ converge to 0. Moreover, $P_{I_{out}} + P_{Z_{out}} \rightarrow 1$.

Therefore,

$$a_n + d_n = 1 \quad (75)$$

$$b_n = 0 \quad (76)$$

$$c_n = 0 \quad (77)$$

So,

$$a_{n+1} = \frac{a_n^2 + d_n^2}{(a_n + d_n)^2 + (b_n + c_n)^2} = \frac{a_n^2 + d_n^2}{(a_n + d_n)^2} \quad (78)$$

$$d_{n+1} = \frac{2a_n d_n}{(a_n + d_n)^2 + (b_n + c_n)^2} = \frac{2a_n d_n}{(a_n + d_n)^2} \quad (79)$$

Let $r = \frac{d}{a}$,

$$r_{n+1} = \frac{2a_n d_n}{a_n^2 + d_n^2} = \frac{2\left(\frac{d_n}{a_n}\right)}{1 + \left(\frac{d_n}{a_n}\right)^2} = \frac{2r_n}{1 + r_n^2} \quad (80)$$

Because $r_0 = \frac{d_0}{a_0}$, we have $0 < r_0 < 1$. Therefore, $0 < \frac{2r_n}{1+r_n^2} < 1$, and hence $0 < r_{n+1} < 1$. Let $q = \frac{1-r}{1+r}$. Thus, $0 < q_n < 1$.

Therefore,

$$q_{n+1} = \frac{1 - r_{n+1}}{1 + r_{n+1}} = \frac{\frac{1+r_n^2-2r_n}{1+r_n^2}}{\frac{1+r_n^2+2r_n}{1+r_n^2}} = \left(\frac{1-r_n}{1+r_n}\right)^2 = q_n^2 \quad (81)$$

Since $0 < q_n < 1$, we have $q_n \rightarrow 0$ as $n \rightarrow \infty$.

So,

$$\begin{aligned} q_n &= \frac{1 - r_n}{1 + r_n} \\ q_n(1 + r_n) &= 1 - r_n \\ q_n + q_n r_n &= 1 - r_n \\ r_n(q_n + 1) &= 1 - q_n \\ r_n &= \frac{1 - q_n}{1 + q_n} \rightarrow 1 \end{aligned}$$

Therefore,

$$\frac{d_n}{a_n} = 1 \quad (82)$$

$$a_n = d_n \quad (83)$$

Since $a_n + d_n = 1$, we have $a_n = d_n = 0.5$.

Therefore, for BBPSSW (no twirl), as $n \rightarrow \infty$, we have

$$a_{n+1} + d_{n+1} = 1 \quad (84)$$

$$b_n + c_n = 0 \quad (85)$$

$$a_{n+1} = \frac{a_n^2 + d_n^2}{(a_n + d_n)^2} = 0.5 \quad (86)$$

$$d_{n+1} = \frac{2a_n d_n}{(a_n + d_n)^2} = 0.5 \quad (87)$$

$$b_n = 0 \quad (88)$$

$$c_n = 0 \quad (89)$$

■

B. DEJMPS (no twirl)

In the DEJMPS (no twirl) setting, the analysis is slightly more involved than for BBPSSW (no twirl). As we derive below, the recursion naturally separates into two cases. In the n th round, the improvement does not always come from the $(n-1)$ st round. In some cases, it comes from the $(n-2)$ nd round. As a result, DEJMPS (no twirl) may converge to 0 more slowly than BBPSSW (no twirl) for the X , Y , and Z components.

For DEJMPS (no twirl), the main text gives the following relationship:

$$P_I = P_{I_{in}}^2 + P_{Y_{in}}^2, \quad (90)$$

$$P_X = P_{X_{in}}^2 + P_{Z_{in}}^2, \quad (91)$$

$$P_Y = 2P_{X_{in}} P_{Z_{in}}, \quad (92)$$

$$P_Z = 2P_{I_{in}} P_{Y_{in}}, \quad (93)$$

$$P_T = P_I + P_X + P_Y + P_Z, \quad (94)$$

$$P_{I_{out}} = \frac{P_I}{P_T}, \quad (95)$$

$$P_{X_{out}} = \frac{P_X}{P_T}, \quad (96)$$

$$P_{Y_{out}} = \frac{P_Y}{P_T}, \quad (97)$$

$$P_{Z_{out}} = \frac{P_Z}{P_T}. \quad (98)$$

Using this, we want to analytically derive the performance that is observed in Fig. 14.

Proof of Theorem 2: Recall that

$$a_0 > \frac{1}{2},$$

$$b_0 > 0, c_0 > 0, d_0 > 0,$$

$$a_0 + b_0 + c_0 + d_0 = 1,$$

$$P_{I_n} = a_n^2 + c_n^2,$$

$$P_{X_n} = b_n^2 + d_n^2,$$

$$P_{Y_n} = 2b_n d_n,$$

$$P_{Z_n} = 2a_n c_n,$$

$$P_{T_n} = P_{I_n} + P_{X_n} + P_{Y_n} + P_{Z_n},$$

$$a_{n+1} = \frac{P_{I_n}}{P_{T_n}},$$

$$b_{n+1} = \frac{P_{X_n}}{P_{T_n}},$$

$$c_{n+1} = \frac{P_{Y_n}}{P_{T_n}},$$

$$d_{n+1} = \frac{P_{Z_n}}{P_{T_n}}.$$

To prove the result, we first derive the following relationship:

$$P_{I_0} = a_0^2 + c_0^2 \quad (99)$$

$$P_{X_0} = b_0^2 + d_0^2 \quad (100)$$

$$P_{Y_0} = 2b_0d_0 \quad (101)$$

$$P_{Z_0} = 2a_0c_0 \quad (102)$$

$$\begin{aligned} P_{T_0} &= P_{I_0} + P_{X_0} + P_{Y_0} + P_{Z_0} \\ &= a_0^2 + c_0^2 + b_0^2 + d_0^2 + 2b_0d_0 + 2a_0c_0 \\ &= (a_0 + c_0)^2 + (b_0 + d_0)^2 \end{aligned}$$

$$a_1 = \frac{a_0^2 + c_0^2}{(a_0 + c_0)^2 + (b_0 + d_0)^2} \quad (103)$$

$$b_1 = \frac{b_0^2 + d_0^2}{(a_0 + c_0)^2 + (b_0 + d_0)^2} \quad (104)$$

$$c_1 = \frac{2b_0d_0}{(a_0 + c_0)^2 + (b_0 + d_0)^2} \quad (105)$$

$$d_1 = \frac{2a_0c_0}{(a_0 + c_0)^2 + (b_0 + d_0)^2} \quad (106)$$

So,

$$a_1 + d_1 = \frac{(a_0 + c_0)^2}{(a_0 + c_0)^2 + (b_0 + d_0)^2} \quad (107)$$

$$b_1 + c_1 = \frac{(b_0 + d_0)^2}{(a_0 + c_0)^2 + (b_0 + d_0)^2} \quad (108)$$

To prepare for the case split in the proof below, we first need to show that $a_1 > \frac{1}{2}$. Note that $a_0 + b_0 + c_0 + d_0 = 1$.

$$\begin{aligned} a_0 &> \frac{1}{2} \\ a_0 &> 1 - a_0 \\ a_0 - c_0 &> 1 - a_0 - c_0 \\ a_0 - c_0 &> b_0 + d_0 \\ (a_0 - c_0)^2 &> (b_0 + d_0)^2 \\ a_0^2 - 2a_0c_0 + c_0^2 &> (b_0 + d_0)^2 \\ 2a_0^2 + 2c_0^2 &> a_0^2 + 2a_0c_0 + c_0^2 + (b_0 + d_0)^2 \\ 2(a_0^2 + c_0^2) &> (a_0 + c_0)^2 + (b_0 + d_0)^2 \\ \frac{a_0^2 + c_0^2}{(a_0 + c_0)^2 + (b_0 + d_0)^2} &> \frac{1}{2} \\ a_1 &> \frac{1}{2} \end{aligned} \quad (109)$$

Next, we apply the same analysis as in BBPSSW (no twirl) to DEJMPS (no twirl).

Let $s = a + c$, $t = b + d$,

$$a_1 + d_1 = \frac{s_0^2}{s_0^2 + t_0^2} \quad (110)$$

$$b_1 + c_1 = \frac{t_0^2}{s_0^2 + t_0^2} \quad (111)$$

So,

$$s_1 = a_1 + c_1 = \frac{s_0^2}{s_0^2 + t_0^2} - d_1 + c_1 \quad (112)$$

$$t_1 = b_1 + d_1 = \frac{t_0^2}{s_0^2 + t_0^2} - c_1 + d_1 \quad (113)$$

Thus,

$$s_1 = a_1 + c_1 = \frac{s_0^2 - 2a_0c_0 + 2b_0d_0}{s_0^2 + t_0^2} \quad (114)$$

$$t_1 = b_1 + d_1 = \frac{t_0^2 - 2b_0d_0 + 2a_0c_0}{s_0^2 + t_0^2} \quad (115)$$

Let $u = \frac{s}{t}$,

$$u_1 = \frac{s_1}{t_1} = \frac{s_0^2 - 2a_0c_0 + 2b_0d_0}{t_0^2 - 2b_0d_0 + 2a_0c_0} \quad (116)$$

$$= \frac{s_0^2}{t_0^2} + \frac{s_0^2 - 2a_0c_0 + 2b_0d_0}{t_0^2 - 2b_0d_0 + 2a_0c_0} - \frac{s_0^2}{t_0^2} \quad (117)$$

$$= \frac{s_0^2}{t_0^2} + \frac{t_0^2(-2a_0c_0 + 2b_0d_0) - s_0^2(-2b_0d_0 + 2a_0c_0)}{t_0^2((b_0 + d_0)^2 - 2b_0d_0 + 2a_0c_0)} \quad (118)$$

$$= u_0^2 + \frac{2(t_0^2 + s_0^2)(b_0d_0 - a_0c_0)}{t_0^2(b_0^2 + d_0^2 + 2a_0c_0)} \quad (119)$$

So,

$$\begin{aligned} u_n &= u_{n-1}^2 + \frac{2(t_{n-1}^2 + s_{n-1}^2)(b_{n-1}d_{n-1} - a_{n-1}c_{n-1})}{t_{n-1}^2(b_{n-1}^2 + d_{n-1}^2 + 2a_{n-1}c_{n-1})} \\ &= u_{n-1}^2 + o(b_{n-1}d_{n-1} - a_{n-1}c_{n-1}) \end{aligned} \quad (120)$$

$$= u_{n-1}^2 + o(b_{n-1}d_{n-1} - a_{n-1}c_{n-1}) \quad (121)$$

Because $2(t_{n-1}^2 + s_{n-1}^2) > 0$ and $t_{n-1}^2(b_{n-1}^2 + d_{n-1}^2 + 2a_{n-1}c_{n-1}) > 0$, the term $(b_{n-1}d_{n-1} - a_{n-1}c_{n-1})$ determines the sign of the second component.

Because the first component already contains u_{n-1}^2 , if the second component is always positive, we can conclude that, when $u_0 > 1$ and $n \rightarrow \infty$, we have $u_n \rightarrow \infty$.

Now, we consider the three cases separately.

In the first case, when $b_{n-1}d_{n-1} - a_{n-1}c_{n-1} > 0$, we can directly conclude that, if $u_0 > 1$ and $n \rightarrow \infty$, then $u_n \rightarrow \infty$.

In the second case, when $b_{n-1}d_{n-1} - a_{n-1}c_{n-1} = 0$, we obtain

$$u_n = u_{n-1}^2 = u_0^{2^n} \quad (122)$$

Therefore, when $u_0 > 1$ and $n \rightarrow \infty$, we have $u_n \rightarrow \infty$.

In the third case, when $b_{n-1}d_{n-1} - a_{n-1}c_{n-1} < 0$, the analysis becomes slightly more subtle. In this case, u_n does not necessarily improve from u_{n-1} , but may instead improve from u_{n-2} .

First, it does not necessarily improve from u_{n-1} . Note that $t_0 + s_0 = 1$.

$$u_1 = \frac{s_0}{t_0} + \frac{s_0^2 - 2a_0c_0 + 2b_0d_0}{t_0^2 - 2b_0d_0 + 2a_0c_0} - \frac{s_0}{t_0} \quad (123)$$

$$= \frac{s_0}{t_0} + \frac{t_0(s_0^2 - 2a_0c_0 + 2b_0d_0) - s_0(t_0^2 - 2b_0d_0 + 2a_0c_0)}{t_0((b_0 + d_0)^2 - 2b_0d_0 + 2a_0c_0)} \quad (124)$$

$$= u_0 + \frac{t_0s_0(s_0 - t_0) + 2(t_0 + s_0)(b_0d_0 - a_0c_0)}{t_0^2(b_0^2 + d_0^2 + 2a_0c_0)} \quad (125)$$

$$= u_0 + \frac{t_0s_0(2s_0 - 1) + 2(b_0d_0 - a_0c_0)}{t_0^2(b_0^2 + d_0^2 + 2a_0c_0)} \quad (126)$$

When $b_0d_0 - a_0c_0 < 0$, the quantity $t_0s_0(2s_0 - 1) + 2(b_0d_0 - a_0c_0)$ may also be negative. For example, for $a_0 = 0.7$ and $b_0 = c_0 = d_0 = 0.1$, it is less than 0.

Second, it can improve from u_{n-2} .

$$u_{n-1} = u_{n-2}^2 + \frac{2(t_{n-2}^2 + s_{n-2}^2)(b_{n-2}d_{n-2} - a_{n-2}c_{n-2})}{t_{n-2}^2(b_{n-2}^2 + d_{n-2}^2 + 2a_{n-2}c_{n-2})} \quad (127)$$

$$u_n = (u_{n-2}^2 + o_1(b_{n-2}d_{n-2} - a_{n-2}c_{n-2}))^2 \quad (128)$$

$$+ o_2(b_{n-1}d_{n-1} - a_{n-1}c_{n-1}) \quad (129)$$

Based on numerical simulations, we found that u_n may not always show an obvious improvement over u_{n-2} . However, we observed that u_n always shows an obvious improvement over u_{n-m} for some m .

We tried different initial conditions and consistently observed that the sequence eventually starts increasing more clearly, but the iteration index at which this increase begins depends on the initial conditions. We observe this behavior numerically, but we do not yet know how to prove it mathematically.

Therefore, when $u_0 > 1$ and $n \rightarrow \infty$, we have $u_n \rightarrow \infty$.

Since $u_0 > 1$ implies $s_0 > t_0$, it follows that $F_{I_{in}} + F_{Y_{in}} > F_{X_{in}} + F_{Z_{in}}$. Moreover, as discussed in the main text, $F_{I_{in}} > 0.5$. Therefore, the condition $u_0 > 1$ is always satisfied.

Therefore, as $n \rightarrow \infty$, we have $u_n = \frac{s_n}{t_n} \rightarrow \infty$.

So,

$$a_{n+1} + d_{n+1} = \frac{s_n^2}{s_n^2 + t_n^2} = \frac{(\frac{s_n}{t_n})^2}{(\frac{s_n}{t_n})^2 + 1} = \frac{(u_n)^2}{(u_n)^2 + 1} \rightarrow 1 \quad (130)$$

$$b_{n+1} + c_{n+1} = \frac{t_n^2}{s_n^2 + t_n^2} = \frac{1}{(\frac{s_n}{t_n})^2 + 1} = \frac{1}{(u_n)^2 + 1} \rightarrow 0 \quad (131)$$

Therefore, as $n \rightarrow \infty$, we have $b_{n+1} + c_{n+1} \rightarrow 0$, and hence $P_{X_{out}}$ and $P_{Y_{out}}$ converge to 0. Moreover, $P_{I_{out}} + P_{Z_{out}} \rightarrow 1$.

Therefore,

$$a_n + d_n = 1 \quad (132)$$

$$b_n = 0 \quad (133)$$

$$c_n = 0 \quad (134)$$

So,

$$a_{n+1} = \frac{a_n^2 + c_n^2}{(a_n + c_n)^2 + (b_n + d_n)^2} = \frac{a_n^2 + c_n^2}{(a_n + c_n)^2} = 1 \quad (135)$$

$$d_{n+1} = \frac{2a_n c_n}{(a_n + c_n)^2 + (b_n + d_n)^2} = \frac{2a_n c_n}{(a_n + c_n)^2} = 0 \quad (136)$$

Therefore, for DEJMPS (no twirl), as $n \rightarrow \infty$, we have

$$a_{n+1} + d_{n+1} = 1 \quad (137)$$

$$b_n + c_n = 0 \quad (138)$$

$$a_{n+1} = \frac{a_n^2 + c_n^2}{(a_n + c_n)^2} = 1 \quad (139)$$

$$d_{n+1} = \frac{2a_n c_n}{(a_n + c_n)^2} = 0 \quad (140)$$

$$b_n = 0 \quad (141)$$

$$c_n = 0 \quad (142)$$

Recall that, for BBPSSW (no twirl), as $n \rightarrow \infty$, we have

$$a_{n+1} + d_{n+1} = 1 \quad (143)$$

$$b_n + c_n = 0 \quad (144)$$

$$a_{n+1} = \frac{a_n^2 + d_n^2}{(a_n + d_n)^2} = 0.5 \quad (145)$$

$$d_{n+1} = \frac{2a_n d_n}{(a_n + d_n)^2} = 0.5 \quad (146)$$

$$b_n = 0 \quad (147)$$

$$c_n = 0 \quad (148)$$

We observe that, after the Y and Z swap in DEJMPS (no twirl), the evolution of the I and Z components, which was previously dominated by Z , becomes dominated by Y . Moreover, since Y converges to 0 strictly, the modified dynamics in DEJMPS(no twirl) drives Z to 0, and hence I converges to 1.

■